Cell Metabolism

Article

The Nuclear Receptor ESRRA Protects from Kidney Disease by Coupling Metabolism and Differentiation

Graphical Abstract

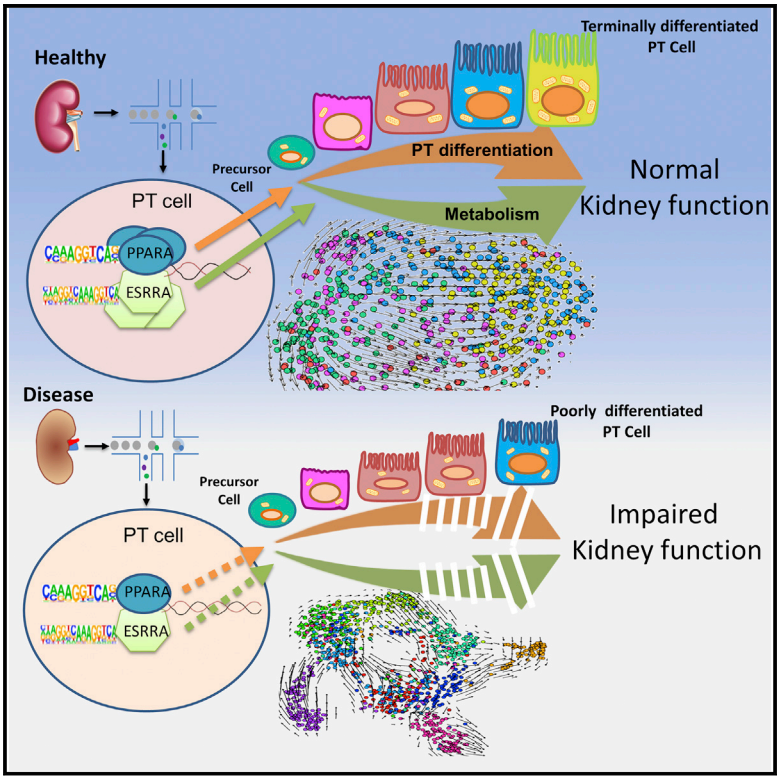

Highlights

- scRNA-seq analysis identified 30 cell types in mouse models of renal fibrosis
- PTs are highly vulnerable to dysfunction diseased kidneys
- PT cell differentiation is altered in renal fibrosis
- ESRRA protects from renal disease by coupling PT metabolism and differentiation

Authors

Poonam Dhillon, Jihwan Park, Carmen Hurtado del Pozo, ..., Junhyong Kim, Nuria Montserrat, Katalin Susztak

Correspondence

jihwan.park@gist.ac.kr (J.P.), nmontserrat@ibecbarcelona.eu (N.M.), ksusztak@pennmedicine.upenn.edu (K.S.)

In Brief

Using single-cell RNA sequencing, Susztak and colleagues, show major changes in cell diversity in mouse models of kidney fibrosis. Proximal tubule (PT) cells are highly vulnerable to dysfunction in fibrosis and show altered differentiation. Nuclear receptors such as ESRRA maintain both PT cell metabolism and differentiation by directly regulating PT-cell-specific genes.

Dhillon et al., 2021, Cell Metabolism *33*, 379–394
February 2, 2021
https://doi.org/10.1016/j.cmet.2020.11.011

CellPress

Cell Metabolism

CellPress

Article

The Nuclear Receptor ESRRA Protects from Kidney Disease by Coupling Metabolism and Differentiation

Poonam Dhillon,[1,2,14] Jihwan Park,[1,2,3,14,*] Carmen Hurtado del Pozo,[4] Lingzhi Li,[1,2] Tomohito Doke,[1,2] Shizheng Huang,[1,2] Juanjuan Zhao,[10] Hyun Mi Kang,[1,2,13] Rojesh Shrestra,[1,2] Michael S. Balzer,[1,2] Shatakshee Chatterjee,[1,2] Patricia Prado,[4] Seung Yub Han,[5] Hongbo Liu,[1,2] Xin Sheng,[1,2] Pieterjan Dierickx,[2] Kirill Batmanov,[1,2] Juan P. Romero,[6,7,8] Felipe Prósper,[6,7,8] Mingyao Li,[9] Liming Pei,[2,10] Junhyong Kim,[5] Nuria Montserrat,[4,11,12,*] and Katalin Susztak[1,2,15,*]

[1]Renal, Electrolyte, and Hypertension Division, Department of Medicine, University of Pennsylvania, Perelman School of Medicine, Philadelphia, PA 19104, USA

[2]Institute for Diabetes, Obesity, and Metabolism, University of Pennsylvania, Perelman School of Medicine, Philadelphia, PA 19104, USA

[3]School of Life Sciences, Gwangju Institute of Science and Technology (GIST), 123 Cheomdangwagi-ro, Buk-gu, Gwangju, Republic of Korea

[4]Pluripotency for Organ Regeneration, Institute for Bioengineering of Catalonia (IBEC), The Barcelona Institute of Technology (BIST), Barcelona, Spain

[5]Department of Biology, University of Pennsylvania, Philadelphia, PA 19104, USA

[6]Cell Therapy Program, Center for Applied Medical Research (CIMA), University of Navarra, Pamplona, Spain

[7]Oncohematology Program, Center for Applied Medical Research (CIMA), University of Navarra, Pamplona, Spain

[8]Hematology and Area of Cell Therapy, Clínica Universidad de Navarra, University of Navarra, Pamplona, Spain

[9]Department of Epidemiology and Biostatistics, University of Pennsylvania, Perelman School of Medicine, Philadelphia, PA 19104, USA

[10]Center for Mitochondrial and Epigenomic Medicine, Department of Pathology and Laboratory Medicine, Children's Hospital of Philadelphia, Perelman School of Medicine, University of Pennsylvania, Philadelphia, PA 19104, USA

[11]Catalan Institution for Research and Advanced Studies (ICREA), Barcelona, Spain

[12]Centro de Investigación Biomédica en Red en Bioingeniería, Biomateriales y Nanomedicina, Madrid, Spain

[13]Laboratory of Disease Modeling and Therapeutics, Korea Research Institute of Bioscience and Biotechnology, Daejeon, Republic of Korea

[14]These authors contributed equally

[15]Lead Contact

*Correspondence: jihwan.park@gist.ac.kr (J.P.), nmontserrat@ibecbarcelona.eu (N.M.), ksusztak@pennmedicine.upenn.edu (K.S.)

https://doi.org/10.1016/j.cmet.2020.11.011

SUMMARY

Kidney disease is poorly understood because of the organ's cellular diversity. We used single-cell RNA sequencing not only in resolving differences in injured kidney tissue cellular composition but also in cell-type-specific gene expression in mouse models of kidney disease. This analysis highlighted major changes in cellular diversity in kidney disease, which markedly impacted whole-kidney transcriptomics outputs. Cell-type-specific differential expression analysis identified proximal tubule (PT) cells as the key vulnerable cell type. Through unbiased cell trajectory analyses, we show that PT cell differentiation is altered in kidney disease. Metabolism (fatty acid oxidation and oxidative phosphorylation) in PT cells showed the strongest and most reproducible association with PT cell differentiation and disease. Coupling of cell differentiation and the metabolism was established by nuclear receptors (estrogen-related receptor alpha [ESRRA] and peroxisomal proliferation-activated receptor alpha [PPARA]) that directly control metabolic and PT-cell-specific gene expression in mice and patient samples while protecting from kidney disease in the mouse model.

INTRODUCTION

Kidney disease is becoming a major health issue in modern society. Chronic kidney disease (CKD) is the tenth leading cause of death worldwide with a steadily increasing incidence affecting eight hundred million people globally (Levin et al., 2017). The increase in the number of people affected by CKD is of concern because it is associated with an increased risk of death and progression to end-stage renal disease (ESRD). In addition, kidney disease is a massive personal and societal economic burden (Breyer and Susztak, 2016; Kovesdy et al., 2013).

Genetic studies examining the heritability of kidney function, such as integration of genome-wide association studies (GWAS) (Wuttke et al., 2019) and functional genomic studies, highlighted the role of proximal tubule (PT)-specific genes in kidney function (Hellwege et al., 2019; Park et al., 2018; Qiu et al., 2018). PT cells are highly susceptible to toxic and hypoxic injury, representing the primary cause of acute kidney injury (AKI) (Qiu et al., 2018). PT-cell-specific injury observed in AKI probably has the most rapid effect on kidney function. CKD is characterized by PT cell atrophy almost independent of disease etiology. PT cell atrophy strongly correlates with kidney function in CKD (Chang-Panesso and Humphreys,

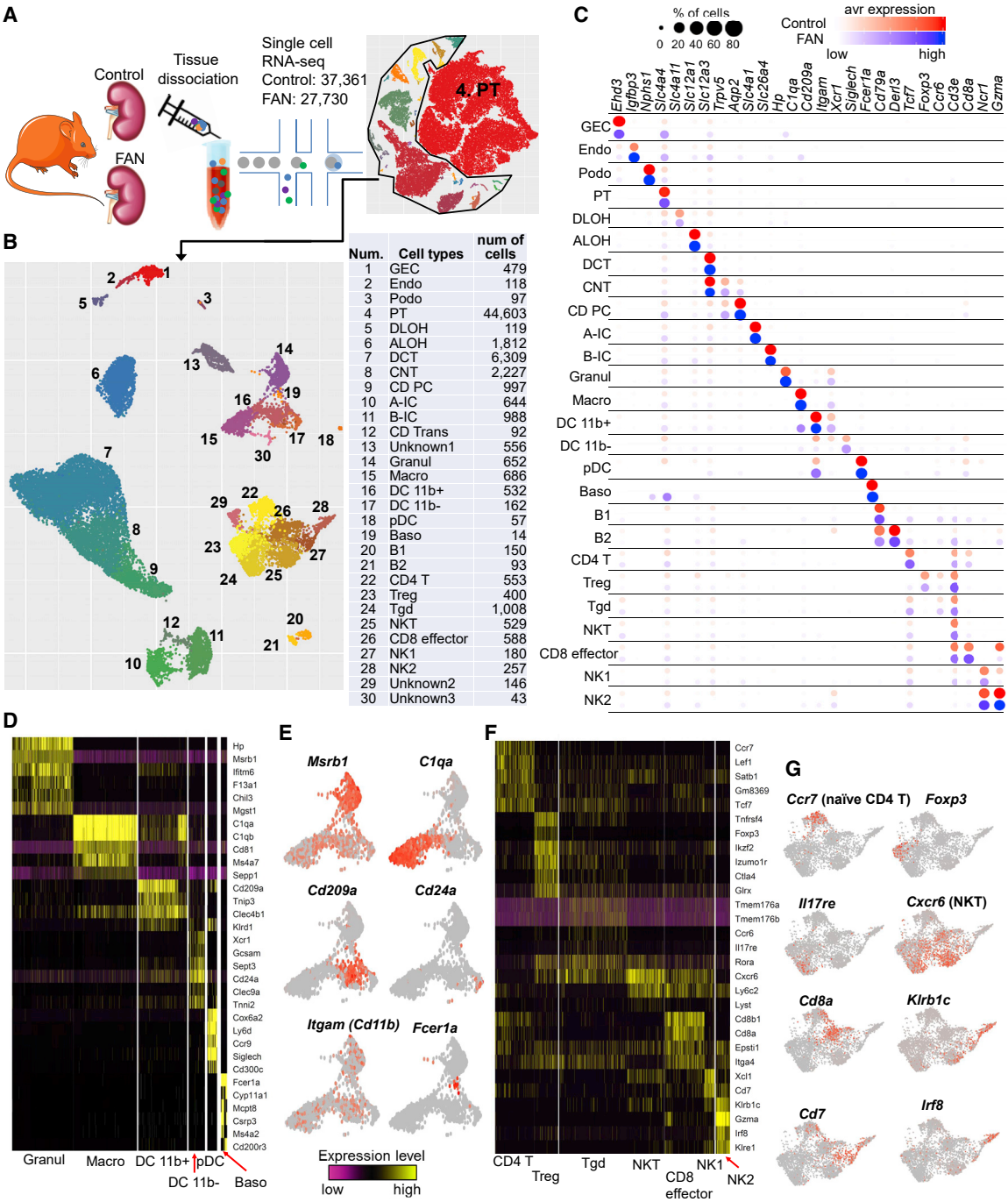

Figure 1. The Cellular Diversity of Diseased Kidney Samples

(A) A schematic diagram illustrating the experimental procedure involving the digestion of whole-kidney tissue from 6 control and 2 FAN mice followed by sequencing using a 10X Genomics protocol and transcriptomic analysis of 65,091 individual cells.

(B) Left, the UMAP of 29 distinct cell types identified by unsupervised clustering after excluding PT cells. Right, the tSNE (t-distributed stochastic neighbor embedding) plot for the entire dataset including PT cells. Assigned cell types are summarized in the right panel. GEC, glomerular endothelial cells; Endo, endothelial; Podo, podocyte; PT, proximal tubule; DLOH, descending loop of Henle; ALOH, ascending loop of Henle; DCT, distal convoluted tubule; CNT, connecting tubule; CD-PC, collecting duct principal cell; A-IC, alpha intercalated cell; B-IC, beta intercalated cell; CD-trans. collecting duct transitional cell; Granul, granulocyte; Macro, macrophage; DC 11b+, CD11b+ dendritic cell; pDC, plasmacytoid DC; Baso, basophile B, B lymphocyte; Treg, regulatory T cell; Tgd, gamma Delta T cell, and; NK, natural killer cell.

(C) Bubble plots of cell cluster marker genes identified in control and FAN samples (size of the dot indicates the % positive cells, color indicates relative expression).

(D) Heatmap showing expression pattern of myeloid lineage markers.

(legend continued on next page)

2017; Reidy et al., 2014) (Liu et al., 2014) (Kang et al., 2015; Li et al., 2012).

Comprehensive genome-wide kidney tissue transcriptomics analysis has been used to define the molecular hallmarks of CKD, both in patient samples and mouse models (Beckerman et al., 2017; Qiu et al., 2018; Woroniecka et al., 2011). These studies highlighted a correlation between a large number of transcripts and kidney fibrosis. Cellular metabolism such as genes involved in lipid metabolism, fatty acid oxidation (FAO), and oxidative phosphorylation (OXPHOS) showed a strong correlation with disease state, both in patients and mouse CKD models (Chung et al., 2019; Kang et al., 2015). Pharmacological or genetic approaches that enhance FAO and mitochondrial biogenesis improved kidney function; however, the exact mechanism is not fully understood (Gomez et al., 2015; Tran et al., 2011; Tran et al., 2016; Zheng et al., 2019). Mitochondrial defects can also lead to the leakage of the mitochondrial DNA into the cytoplasm, resulting in the activation of the cyclic GMP–AMP synthase (cGAS) and stimulator of interferon genes(STING) innate immune system pathways, cytokine release, and influx of immune cells and downstream fibrosis development (Chung et al., 2019; Maekawa et al., 2019).

Single-cell RNA sequencing (scRNA-seq) analysis is transforming our understanding of complex diseases. In our previous study, we identified 21 distinct cell types, including three novel cell types in the kidney (Park et al., 2018). At the same time, we defined cell identity genes that can stably and reproducibly classify key kidney cell types in mice and humans (Menon et al., 2020; Young et al., 2018).

Here, we analyzed the transcriptome of different CKD mouse models, human kidney samples, and human organoids. Prior studies mostly relied on single nuclear sequencing and did not properly capture immune cell diversity (Lake et al., 2019; Wu et al., 2019). We identify several PT cell subgroups, and using cell trajectory analyses, we show an alteration in the differentiation state of PT cells in diseased kidneys. Single-cell epigenetics and transcriptomics indicate the critical role of HNF4A and HNF1B (hepatocyte nuclear factor 4A and 1B), PPARA (peroxisomal proliferation-activated receptor alpha), and ESRRA (estrogen-related receptor alpha) in defining PT cell identity. Using mouse knock out and human kidney transcriptomics data, we demonstrate the protective role of ESRRA, which links energy metabolism, PT differentiation, and kidney function by directly binding to PT-cell-specific genes regulating their expression.

RESULTS

The Single-Cell Landscape Shows Increased Cellular Heterogeneity in Fibrotic Kidneys

To unravel cellular changes associated with kidney fibrosis, we first analyzed the transcriptome of 65,091 individual cells from 6 mouse control kidneys and 2 folic acid (FA)-induced fibrotic kidneys (folic acid nephropathy [FAN]) (Figure 1A). This is a well-established kidney disease model that presents both with structural damage (fibrosis) and kidney function decline indicated by serum blood urea nitrogen (BUN) level (Figures S1A–S1C). We observed that PT cells represented the majority of cell types in the dataset. To accurately cluster smaller cell populations, we first focused on non-PT cells (Figure 1B). Our unbiased clustering identified 30 cell populations, including kidney epithelial, immune, and endothelial cells based on marker gene expression (Figures 1C and S1D; Table S1). The proportion of cells were relatively stable in biological replicates but were substantially different between control and FAN samples (Figure S1E). Gene sets previously used to define cell types (cell identity genes) showed conserved expression in the disease state (Figure S1F). Immune cell diversity was markedly increased in the FAN mice (Figures S1D and S1E). We identified 14 immune cell clusters in our FAN model, whereas our previous study characterized 5 immune clusters (Park et al., 2018). Among the newly identified, we observed granulocytes, macrophages, dendritic cells (DCs), and basophils. DCs were further sub-clustered into DC 11b+ (*Cd209a* and *Cd11b*), DC 11b- (*Cd24a* and *Clec9a*), and plasmacytoid DC clusters (*Siglech* and *Cd300c*) (Figures 1D and 1E). A large number of lymphoid cells were also identified, including B cells, T cells, and natural killer (NK) cells (Figures 1B and 1C). T lymphocytes were sub-clustered into $CD4^+$ T, Treg, gamma delta T, NKT, and $CD8^+$ effector cells (Figures 1F and 1G). We made this dataset publicly available on our interactive website (http://susztaklab.com/VisCello/).

Bulk RNA Sequencing Strongly Influenced by Cell Fraction Changes

We next performed RNA-seq of whole-kidney (i.e., bulk tissue) samples, as single-cell sequencing may experience uneven cell drop-out. Differential expression analysis of bulk RNA-seq data indicated changes in expression of more than 4,000 genes (2,776 with higher and 1,361 with lower expression, using false discovery rate [FDR] of 0.05 and 2-fold change) (Figure 2A). Gene ontology analysis highlighted that the expression of genes associated with the immune system and inflammation was higher in the FAN model (Figure 2A). Analysis of genes showing the highest increased expression in the bulk dataset indicated that most of these genes were exclusively expressed by immune cells (Figure 2B). Genes whose levels were lower in the FAN model were enriched for metabolic processes such as lipid metabolism, FAO, and OXPHOS (Figure 2A). Genes with lower expression in the FAN model showed enrichment for PT cell expression (Figure 2B), suggesting a strong role for PT cells and immune cells driving transcriptional changes in bulk RNA-seq data. In addition, we observed that highly expressed and top differentially expressed genes, including *Lyz2*, *Cd52*, and

(E) Gene expression feature plots of myeloid lineage cells projected onto the UMAP. Msrb1 (methionine sulfoxide reductase B1), Granul; C1qa (Complement C1q A Chain), Macro; CD209a (CD209 antigen-like protein A), DC 11b+; CD24a (CD24a antigen), DC 11b-; Itgam (integrin Subunit alpha M), DC 11b+; and Fcer1a (Fc Fragment of IgE Receptor Ia), Baso.

(F) Heatmap showing the expression pattern of lymphoid lineage markers.

(G) Gene expression feature plots of lymphoid lineage cells projected onto the UMAP. *Ccr7* (chemokine C-C motif receptor 7), CD4 T; *Foxp3* (Forkhead Box P3), Treg; *Il-17re* (interleukin-17 receptor E), Tgd; *Cxcr6* (chemokine C–X-C motif receptor 6), NKT; *CD8a* (CD8 antigen, alpha chain), CD8 effector; *Klrb1c* (Killer cell lectin-like receptor subfamily B member 1C), NK1-2; *CD7* (CD7 antigen), NK1, and; *Irf-8* (interferon regulatory factor-8), NK2

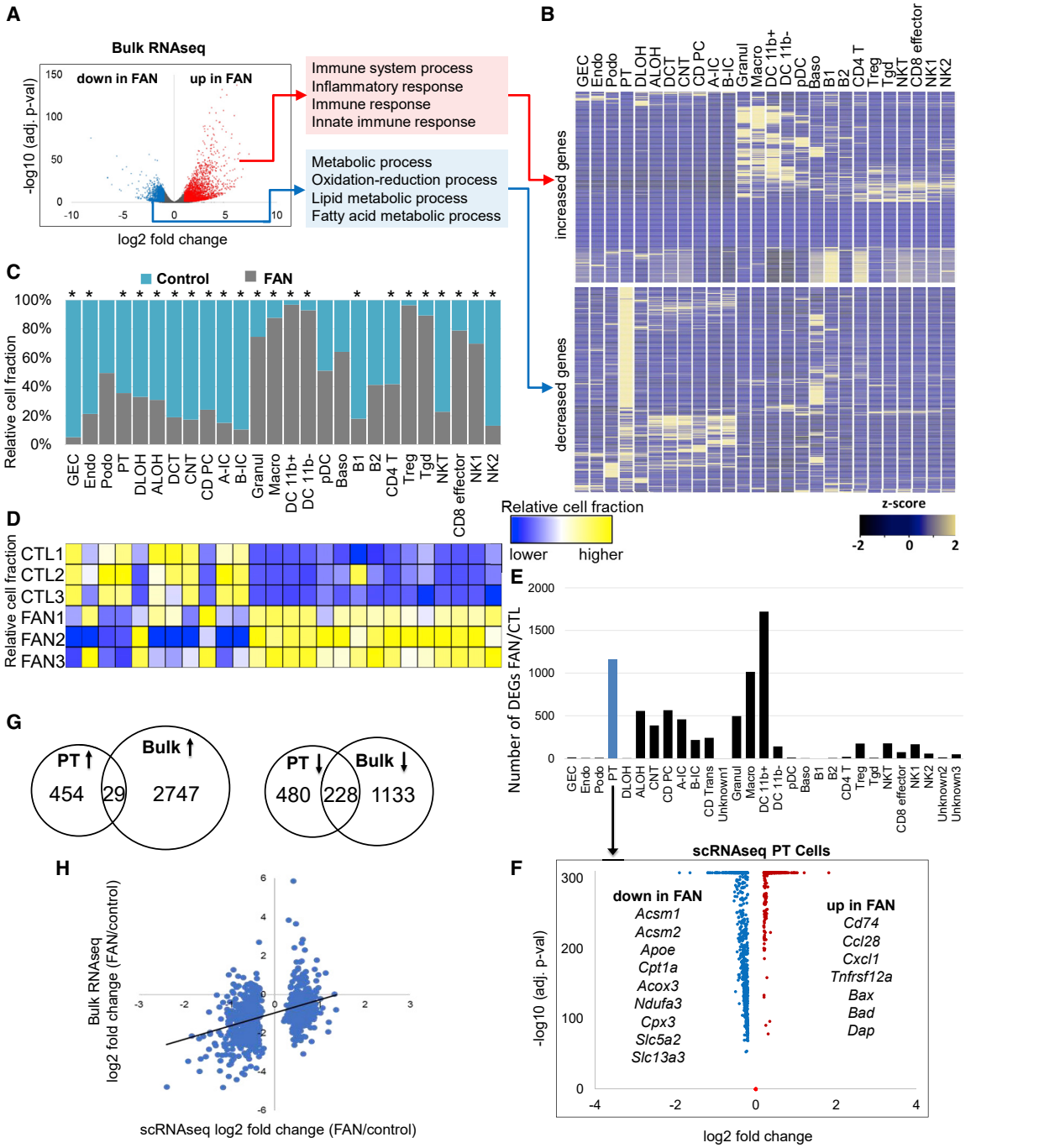

Figure 2. Cell Composition and Cell-Type-Specific Changes in Kidney Fibrosis

(A) DEGs in whole kidneys of control and FAN mice. Volcano plot: the x axis indicates log_2-fold change and y axis indicates statistical significance adjusted p = –log10. Gene ontology analysis of genes showing higher (red) and lower (blue) in FAN kidneys.

(B) Cell-type-specific expression of top DEGs identified in bulk RNA-seq analysis in the single-cell dataset. Mean expression values of the genes were calculated in each cluster. The color scheme is based on *Z* score distribution.

(C) Cell proportion changes in control and FAN kidneys revealed by scRNA-seq. * indicates significant changes by proportion test.

(D) Cell proportion changes revealed by *in silico* deconvolution of bulk RNA-seq data.

(E) The numbers of cell-type-specific differentially expressed genes identified in control FAN kidneys in the 30 cell clusters.

(F) Volcano plot for DEGs between control and FAN PTs identified in the single-cell data. The x axis is log_2-fold change and y axis is statistical significance adjusted p = –log10.

(legend continued on next page)

Tyrobp, in the bulk RNA-seq data showed similar expression patterns in control and FAN samples at a single-cell level (Figure S2A). This suggests that the majority of genes showing higher expression in disease were related to immune cell proportion changes rather than cell-specific changes.

Next, we determined cell proportion changes using single-cell and bulk RNA-seq data. We found marked differences in cell proportion, such as a distinct increase in the proportion of myeloid and lymphoid cells (e.g., macrophages [7.2-fold], granulocytes [2.9-fold], Tregs [27-fold], and CD8 effector cells [3.8-fold]) but a decrease in the proportion of tubule epithelial cells (e.g., PT [0.55-fold] and distal convoluted tubule [0.23-fold]) in the single-cell data of the FAN model (Figure 2C). In contrast, consistent with prior observations, the proportion of podocytes did not show clear changes in the FAN model (Figure 2C). We also performed *in silico* deconvolution of bulk RNA-seq data implemented in the CellCODE package. This analysis yielded results broadly consistent with the single-cell RNA-seq data (Figure 2D), such as higher immune cell fractions and lower epithelial cell fractions. Finally, cell proportion changes in epithelial and immune cells were confirmed by histological analysis (Figure S1A).

To further understand the contribution of cell-type-specific and cell fraction changes in bulk RNA-seq results, we directly compared the single-cell with the bulk data. After adjusting the data to the observed cell fraction changes, the number of genes showing differential expression was markedly reduced. Among the 4,137 differentially expressed genes in the bulk data, only 14, 2, 902, and 753 genes remained significant after adjustment to the proximal convoluted tubule (PCT), proximal straight tubule (PST), and myeloid or lymphoid cell fractions, respectively (Figure S2B).

To unravel cell-type-specific gene expression changes in the FAN model, we performed differential expression analysis in all identified cell types. Keeping in mind the limitation of this analysis, such as the complete confounding of the disease-state and possible batch effect, we found that myeloid cells such as macrophages showed a large number of differentially expressed genes (Figure 2E). We found that among the epithelial cells, PT cells showed the largest number of differentially expressed genes (Figure 2E; Table S2). Genes that showed lower expression levels in diseased PT cells were solute carriers (cell-differentiation-related genes), such as *Slc5a2* and *Slc13a3*, as well as genes involved in FAO and OXPHOS (e.g., *Acsm1, Acsm2, Cpt1a, Acox3*) (Figure 2F).

Even though PT cells represented a large portion of the bulk dataset, only a fraction of differentially expressed genes observed in PT cells were shared in the bulk RNA-seq data (Figure 2G), and the correlation between the PT-cell-specific differentially expressed genes in the single-cell and bulk data was weak (Figure 2H).

Altered Differentiation Drives Proximal Tubule Response during Fibrosis

To better understand cell state changes in PT cells, we performed sub-clustering and cell trajectory analysis of healthy and diseased samples from CKD mouse models. In healthy controls, we identified several PT cell subtypes, including PST cells expressing *Slc22a30*, and several subgroups of PCT expressing *Slc5a2* and *Slc5a12* (Figure 3A; Table S3). RNA velocity analysis is a new way of studying cellular differentiation (La Manno et al., 2018) by predicting the future state of individual cells. Our analysis indicated that in control kidneys, PT cells differentiated into two major cell types: PCT and PST segments (Figures 3B and 3C). Interestingly, the analysis highlighted that PT cells originated from a common precursor-like cell, expressing higher levels of *Med28* and *Cycs* (Figure 3D). Importantly, our analysis also suggested that PT cell differentiation did not necessitate cell proliferation, as we did not observe changes in the expression of proliferation markers (Figure 3D).

PT cells from FAN samples sub-clustered into nine groups. Using anchor genes to identify key cell types such as PCT and PST segments, we were able to recognize more heterogeneous cell populations, including proliferating cells, immune marker (*Cd74*)-expressing cells, transitional cells, and precursor cells expressing higher *Igfbp7* (Figure 3E; Table S3). In diseased samples, we also identified a prominent proliferating (i.e., *Ki67*-positive) cell population, and it appeared that cells entered and exited this *Ki67*-positive state. These data are consistent with a facultative progenitor model in kidney tubule cells (Angelotti et al., 2012; Kang et al., 2016) (Figure 3F). Notably, we identified a cell population expressing *Notch2* and *Lgr4*, which were previously identified as progenitor and transit-amplifying cells in the kidney and other organs (de Lau et al., 2011; Zhang et al., 2019). We observed that PCT cells co-expressed PST markers, suggesting that under disease conditions, PCT cells may endure transcriptomic changes impacting their phenotypic signature. Similar to our observation in the control samples (Figure 3B), FAN samples showed a differentiation trajectory toward PCT and PST segments (Figures 3G and 3H) but followed a less organized differentiation path than healthy PT cells (Figure 3G). In contrast, we failed to observe a clear reversal of the differentiation of cells already expressing terminal differentiation markers such as *Slc5a2* or *Slc22a30*, indicating that a failure of differentiation rather than dedifferentiation is the reason for the identified cell-state changes.

Differentiation Defects in Fibrotic Proximal Tubules Track with Changes in Lipid Metabolism

Next, we opted to take advantage of the continuous cell trajectory analysis using the Monocle package by combining all samples under healthy and disease states (Trapnell et al., 2014). Initial exploration showed a clear branching of PT cells into PCT and PST segments (Figures 4A, 4B, and S3A), which was mostly consistent with the RNA velocity analysis. To identify genes whose expression changed along the trajectory, we first performed a trajectory analysis for the PST segment, as this segment is highly susceptible to injury (Figures 4C, 4D, and S3B). Cells from control and diseased kidneys seemed to follow a similar linear trajectory toward PST segment differentiation

(G) Venn diagrams showing the overlaps between the identified differentially expressed genes in PT cells by scRNA-seq data and bulk RNA-seq data in control versus FAN kidneys (Up arrow: upregulated genes and down arrow: downregulated genes).
(H) Scatter plot showing the correlation of DEGs identified in PT cells and bulk data. The x axis shows the fold change expression in PT cells in the single-cell data, y axis shows the fold change expression in the whole kidney (bulk) samples.

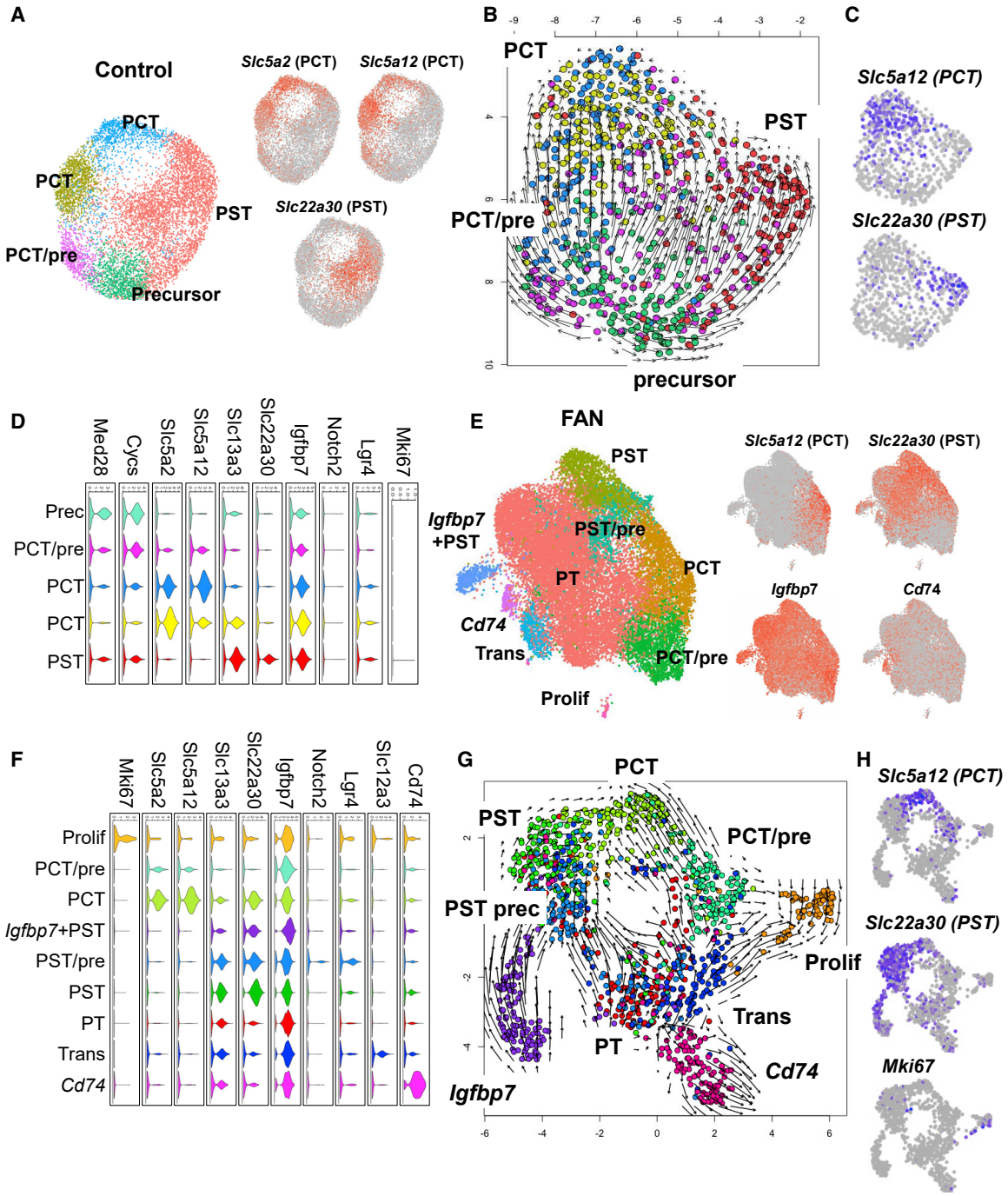

Figure 3. Heterogeneous PT Cell Populations in Fibrotic Kidneys

(A) Sub-clustering of PT cells into five subpopulations in control kidneys. Feature plots showing the expression of key PCT (*Slc5a2* and *Slc5a12*) and PST (*Slc22a30*) segment markers.

(B) RNA velocity analysis of the control of PT cells. Each dot is one cell, and each arrow represents the time derivative of the gene expression state.

(C) Feature plots showing the expression of key PCT (*Slc5a12*) and PST (*Slc22a30*) segment markers in control.

(D) Violin plots showing the expression patterns of markers across PT cell sub-clusters in control. The y axis shows the log-scale normalized read count.

(E) Sub-clustering of PT cells into nine sub-populations in FAN kidneys. Feature plots showing the expression of key PCT (*Slc5a12*) and PST (*Slc22a30*), *Igfbp7* (precursor), and *CD74* (immune) PT cell state markers.

(F) Violin plots showing the expression patterns of markers across PT cell sub-clusters in FAN. The y axis shows the log-scale normalized read count.

(G) RNA velocity analysis of FAN PT cells. Each dot is one cell, and each arrow represents the time derivative of the gene expression state.

(H) Feature plots showing the expression of key PCT (*Slc5a12*) and PST (*Slc22a30*) and proliferating (*Mki67*) PT cell markers.

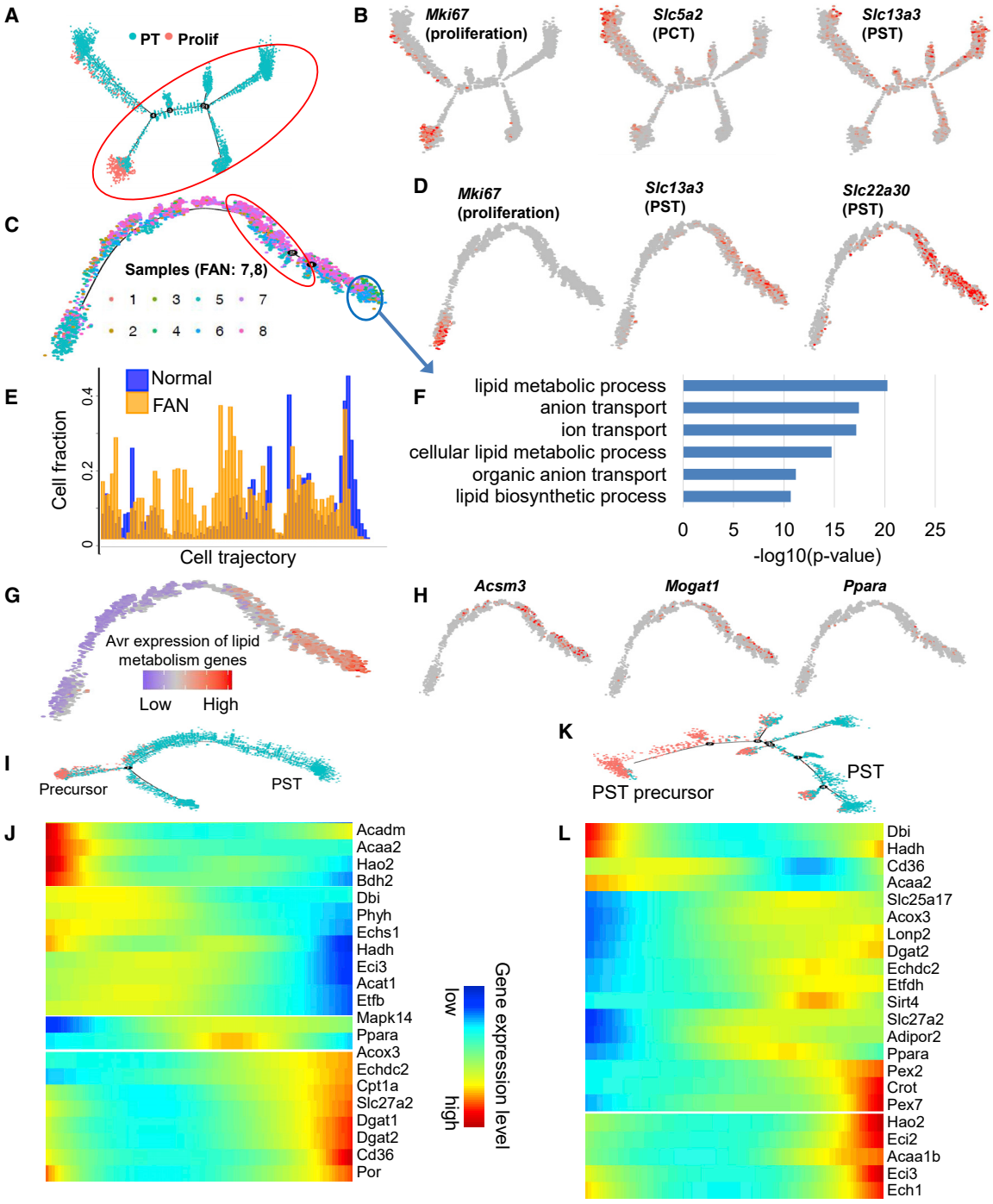

Figure 4. Cell Trajectory Analysis Identifies Differentiation Defect in PT in Fibrosis

(A) trajectory analysis of PT cells (including proliferating cells) using Monocle, including all control and FAN samples.

(B) Feature plots showing the expression levels of key cell state markers (*Mki67*: proliferating cell, *Slc5a2*:PCT, *Slc13a3*:PST) on the cell trajectory.

(C) Cell trajectory analysis focused on the PST cluster (cells under red circle in A). Batches 1–6 represent healthy kidneys, whereas batches 7–8 were obtained from FAN samples.

(D) Feature plots showing the expression levels of key cell state markers (*Mki67*: proliferating cell, *Slc22a30*:PST, *Slc13a3*:PST) on the cell trajectory.

(E) Distributions of cells along the pseudotime trajectory. Note the shift of Normal (blue) and FAN samples (yellow).

(F) Functional annotation (gene ontology) analysis of genes showing changes along the trajectory (cells highlighted by red and blue circles on C).

(G) Average expression levels of the highly variable genes that are involved in lipid metabolism along the cell trajectory.

(H) Feature plots showing the expression levels of the lipid metabolism genes (*Acsm3, Mogat1,* and *Ppara*) along the cell trajectory.

(legend continued on next page)

(i.e., no major branching), but FAN samples were significantly depleted from the terminally differentiated PT cells (two-sample proportion test between cells in the red and blue area, p value < $2.2e^{-16}$) (Figures 4C and 4E). Trajectory analysis of PCT segment cells showed a similar pattern (Figures S3C and S3D). These data are consistent with prior observations, indicating lower levels of terminally differentiated markers in FAN samples (Figure 3G).

When we interrogated genes and pathways that underlie the PT cell differentiation state, we found that the expression of genes associated with terminal differentiation, such as those with ion transport function (i.e., SLCs, solute carriers), increased along the differentiation trajectory (Figure 4F). In addition to ion transport, lipid metabolism showed a positive correlation with cellular differentiation (Figures 4F–4H and S3E). Moreover, we observed changes in FAO genes along the differentiation path from precursor to PT cells in both healthy controls and FAN samples (Figures 4I–4L).

We also generated scRNA-seq data from the unilateral ureteral obstruction (UUO) model of kidney fibrosis and compared cell trajectories in the UUO and the FAN models. Continuous cell trajectory analysis showed a selective lack of terminally differentiated PT cells in UUO kidneys, recapitulating the results obtained from the FAN model (Figures S3F–S3H). In addition, when examining pathways associated with the differentiation of PT cells along the cell trajectory, we found enrichment for FAO, OXPHOS, and ion transport (Figures S3I and S3J). There was a strong (>50%) overlap of gene expression changes along the respective differentiation trajectories in the UUO and FAN models (Figure S3K).

Partial epithelial-mesenchymal transition (EMT) has been used to describe the aberrantly differentiated PT cells (Grande et al., 2015; Lovisa et al., 2015; Zeisberg and Duffield, 2010). We found that EMT markers tended to be lower upon PT cell differentiation (Figure S3L). However, we failed to observe significant expression of *Zeb*, *Twist*, and *Snai* in the different PT cell sub-clusters in fibrotic samples (Table S4). We also failed to observe cells exhibiting classic senescence markers (senescence-associated secretory phenotype [SASP]) (Table S4).

Proximal Tubule Differentiation in Kidney Organoids Correlates with Metabolic Changes

To distinguish whether lipid metabolism and OXPHOS only correlate with PT-cell-specific gene expression or are true drivers of PT cell maturation, we tested the role of FAO and OXPHOS in tubule cell differentiation of developing kidney organoids. Previously, we showed three-dimensional (3D) culture systems that recapitulate architectural and functional features of the human developing kidney, the so-called kidney organoids (Garreta et al., 2019). We generated human pluripotent stem cell (hPSC)s-kidney organoids in free-floating conditions by assembling nephron progenitor cells (NPCs) derived from hPSCs (Figure 5A). Bulk gene expression analysis of differentiating organoids indicated an increase in the expression of *PPARGC1A* on days 16 and 21. The increase in the expression of *PPARGC1A* in organoids correlated with the expression of PT cell markers, such as *SLC27A2*, *SLC3A1*, and *SLC5A12* (Figure 5B). As bulk RNA expression data cannot provide a faithful read-out for PT differentiation, we performed unbiased scRNA-seq analysis (Figure 5C). Clustering analysis based on cell-type-specific marker gene expression indicated that in addition to mesenchymal clusters, we could also identify a variety of kidney cell types resembling those of collecting duct, actively cycling cells, endothelial cells, podocytes, loop of Henle, and PT cells (Figures 5C and 5D). Next, we specifically examined the differentiation trajectory of organoid PT cells. Cells differentiated from a *SIX1* positive progenitor and gained PT cell marker *SLC3A1* expression (Figure 5E). Next, we analyzed genes whose expression changed along this trajectory and found that the expression of differentiation markers such as solute carriers increased along the trajectory and their expression strongly correlated with genes in FAO, including *PPARA* (Figure 5F). Finally, to confirm that FAO is a driver of cellular differentiation, we cultured kidney organoids in the glycolytic-promoting media (EGM, endothelial cell growth medium) or the OXPHOS-promoting media (REGM, renal epithelial cell growth medium). We found higher expression of *PPARGC1A* mRNA and lipid metabolic genes such as *ACOX2, ACOT12*, and *CPT1A*, when organoids were cultured in the REGM media for 4 days versus the EGM media (Figure 5G). We further assessed the protein levels of mitochondrial OXPHOS proteins in organoids exposed to both the REGM and EGM culture media (Figures 5H, S4A, and S4B). Concomitantly to these metabolic changes, we observed that the REGM media led to an increase in the expression of PT cell markers such as *SLC34A1, SLC27A2, SLC5A12*, *SLC6A19*, and *SLC3A1* compared with the EGM media (Figure 5G). These results run in parallel with our *in vitro* observations of cultured PT cells from mice (Figures S4C and S4D). In addition, organoids exhibited a visibly higher number of PTs as observed by immunofluorescence (IF) analysis for Lotus Tetragonolobus Lectin (LTL) labeling (Figures 5I and 5J).

ESRRA Drives Proximal Tubule Differentiation in Mouse Models and Couples Metabolism with Differentiation

In order to define the key transcriptional regulatory organization of PT cells, we analyzed mouse kidney single-cell open chromatin data (scATACseq) (Cao et al., 2018). Using a computation motif search algorithm, we found that the most enriched open binding motifs were HNF4A, HNF1B, PPARA, and ESRRA in PCT and PST cells (Figure 6A). Our single-cell gene expression analysis confirmed transcript enrichment for these 4 transcription factors in PT cells (Figure S5A). Next, we defined putative PPARA and ESRRA target genes by intersecting PCT- or PST-specific open chromatin region at promoters (transcription start site ±5kb) or gene body regions chromatin regions that contained PPARA- or ESRRA-binding motifs. Gene set enrichment analysis showed enrichment for PPARA- and ESRRA-target genes (Table S5) in differentiated PST and PCT cells (Figures

(I) Cell trajectory analysis for PST and precursor clusters identified in control kidneys (Figure 3A).
(J) Heatmap showing the expression changes of highly variable FAO genes along the cell trajectory in control kidneys.
(K) Cell trajectory analysis for PST and precursor clusters identified in FAN samples (Figure 3E).
(L) Heatmap showing the expression changes of highly variable FAO genes along the cell trajectory in FAN samples.

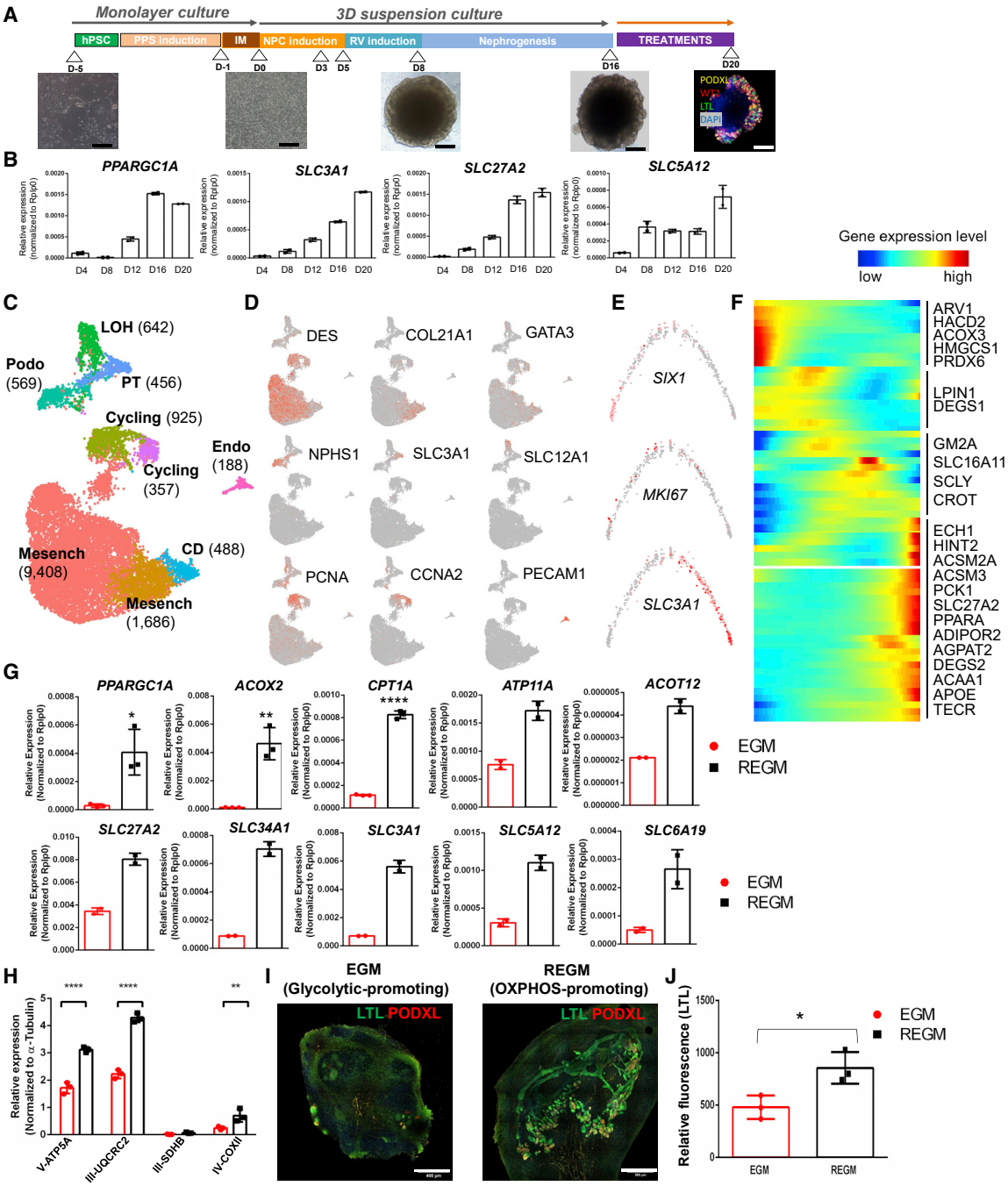

Figure 5. FAO and OXPHOS Drive PT Differentiation in Human Kidney Organoid

(A) Experimental scheme for the generation of human kidney organoid. Briefly, hPSCs were first differentiated into posterior primitive streak (PPS) fate and then into intermediate mesoderm (IM). Cells were aggregated (day 0, D0) and further differentiated in a 3D culture into renal vesicle (RV) and nephron stage. At D20 of differentiated kidney, organoids were stained for podocalyxin (PODXL: podocyte marker, yellow), Wilm's tumor 1 (WT1, red), and Lotus Tetragonolobus Lectin (LTL: PT marker, green). Scale bar, 200 μM.

(B) Transcript expression levels (in bulk organoids) of *PPARGC1A, SLC3A1*, *SLC5A12*, and *SLC27A2* on days 4, 8, 12, 16, and 20 of organoid differentiation. Data are represented as mean ±SEM. n = 2 independent experimental replicates analyzed from a pool of 12 organoids/group.

(C) scRNA-seq analysis of human kidney organoid. UMAP showing nine distinct cell types identified by unsupervised clustering. Mesench, mesenchymal cells; CD, collecting duct; Endo, endothelial cells; cycling, cell cycling cells; Podo, podocytes; LOH, loop of Henle; and PT, proximal tubule.

(D) Feature plots of key cell type markers (*DES, COL21A1, Gata3*; mesenchyme, *NPHS1*; podocytes, *SLC3A1*; PT cell, *SLC12A1*; LOH, PCNA, *CCNA2*; proliferating cells, *PECAM11*; endothelial cells).

(E) Expression of *SIX1* (nephron progenitor marker), *MKI67* (proliferation maker), and *SLC3A1* (PT cell marker) along the differentiation trajectory.

(legend continued on next page)

6B and S5B). PT-specific PPARA and ESRRA target genes were enriched for kidney development, lipid metabolism, and epithelial transport functions (Figures 6C and S5C).

To functionally confirm the role of ESRRA in cellular differentiation, we treated LTL$^+$ PT cells with *Esrra* siRNA or XCT790, a pharmacological inhibitor (inverse agonist) of ESRRA. We observed that reduced *Esrra* activity led to compromised mitochondrial function, as assessed by oxygen consumption rate (OCR) and OXPHOS protein levels as well as decreased mitochondrial DNA content. In addition, reduced *Esrra* led to a lower expression of PT differentiation genes (Figures 6D–6G and S6A–S6D). We next transfected LTL$^+$ PT cells with ESRRA, PPARA, or all four TFs (ESRRA, PPARA, HNF4A, and HNF1B) plasmids. ESRRA overexpression in PT cells not only improved mitochondrial function and mtDNA copy number but also led to an increase in the expression of SLC genes (Figures 6D–6G and S6D–S6F). We found that the overexpression of PPARA, HNF1B, and HNF4A had a synergistic effect as evidenced by the strong additive effect on cellular differentiation, such as the expression of SLCs (Figures S6E and S6F). To establish the role of ESRRA in human PT cell differentiation, we treated human primary renal PT epithelial cells (HPTCs) and kidney organoids cultured in the REGM media with XCT790 for 48 h. Kidney organoids and HPTCs treated with XCT790 showed impaired FAO (Figures S6G and S6I) and reduced expression of SLC genes such as *SLC3A1, SLC27A2, SLC34A1, SLC6A19*, and *ATP11A* (Figures S6G and S6I). Overall, we found that ESRRA inhibition negatively affected PT differentiation as shown by the decreased LTL fluorescence intensity (Figure S6H).

Finally, to distinguish whether ESRRA directly (via binding of the promoter) or indirectly (via improving metabolism) regulated PT cell differentiation, we performed chromatin immunoprecipitation (ChIP) coupled with detection by quantitative real-time PCR (ChIP-qPCR) to study the ESRRA transcription factor binding to DNA in PT cells. We found enrichment for multiple PT-specific genes such as *Slc5a11, Slc6a13, Slc6a19, Slc13a3, Slc7a13, Slc22a6*, and *Slc22a28* and metabolic genes such as *Adipor2* and *Acadm* (Figure 6H).

To define the role of *Esrra* in kidney disease, we challenged *Esrra* knockout (KO) mice with FA (Figure 6I). We found that the expression of *Esrra* was lower in FAN and UUO models of fibrosis when compared with controls (Figures 6I and S6J). We observed that *Esrra* KO mice showed increased susceptibility to FA-induced kidney injury compared with wild-type littermates as detected by histological analysis (Figure S6K). Levels of profibrotic markers such as *Col1a1* and *Col3a1* were higher in FA-treated *Esrra* KO mice (Figure S6L) compared with wild-type counterparts. Animals showed increased collagen accumulation on Sirius red stain (Figure S6M) and increased cell proliferation by Ki67 staining (Figure S6N). We further confirmed the decrease in SLC proteins (SLC6A13 and SLC34A1) and increase in profibrotic proteins (SMA and FN) in *Esrra* KO mice upon FAN injury (Figures 6J and S6O). Further, we found that the genetic deletion of ESRRA in PT cells was associated with impaired mitochondrial function despite the compensatory increase in other nuclear receptors, such as *Esrrg* and *Ppara* (Figures S6P–S6Q), that improved by the re-expression of ESRRA. Similar to prior results, we found that PPARA also regulated PT metabolism and cellular differentiation both *in vitro* and *in vivo* by using fenofibrate: a pharmacologic activator of PPARA (Figures S4C and S5D) (Kang et al., 2015), indicating a likely complex interaction between the different nuclear receptors in PT cells.

ESRRA Driven Metabolic Changes Correlates with Kidney Disease Severity in Patient Samples

Finally, we wanted to ascertain whether ESRRA-driven metabolism and PT cell differentiation that appears to drive disease development in mouse kidney disease models can also be recapitulated in patients with CKD. We analyzed 91 microdissected human kidney tubule samples obtained from healthy subjects and patients with diabetic and hypertensive kidney disease (Table S7). First, we examined the expression of genes involved in FAO and found a group of genes, which strongly correlated with kidney fibrosis (Figure 7A). These genes included *ADIPOR2, PPARA, ACSM2A, ACSM3, and APOE*, for which we had previously demonstrated an increase along the PT differentiation trajectory (Figure 4J). Correlation analysis revealed that the expression of lipid metabolism genes showed a positive correlation with the expression of PT cell differentiation and negative correlation with fibrosis (Figure 7B). *In silico* deconvolution of bulk transcriptome data from 91 human samples showed that the proportion of PCT and PST cells decreased in fibrotic tissues (Figure 7C). Next, we assessed the effect of cell proportion changes on gene expression changes observed in bulk gene profiling data (Figure 7C). Expression of a total of 1,980 genes significantly correlated with fibrosis scores in 91 human kidney samples analyzed by linear regression using age, gender, race, and diabetes and hypertension status as covariates (FDR < 0.05). Next, we performed *in silico* deconvolution analysis of the data using CellCODE. Adjusting the model to the 4 cell lineages (PCT, PST, myeloid, and lymphoid cells) reduced the number of differentially expressed genes (DEGs) from 1,980 to 22 genes, indicating the key role of cell heterogeneity in driving bulk gene expression changes (Figure S7A).

(F) Heatmap showing the expression changes of highly variable genes involved in FAO identified (Figures 4J and 4L) along the organoid cell differentiation trajectory.

(G) Expression level of genes associated with FAO (*PPARGC1A, ACOX2*, and *CPT1A*), and PT cell markers (*ATP11A, ACOX12, SLC27A2, SLC34A1, SLC3A1, SLC5A2*, and *SLC6A19*) in kidney organoids cultured in the EGM and REGM media. The data are represented as mean ±SEM. n ≥ 2 independent experimental replicates from a pool of 12 organoids/group; *p < 0.05, **p < 0.01, ***p < 0.001, and ****p < 0.0001 paired Student's t test.

(H) Quantification of changes in the protein expression of OXPHOS proteins in organoids cultured in the EGM or REGM media. Tubulin is used as loading control. The data are represented as mean ±SEM. n = 3 independent experimental replicates from a pool of 16 organoids/group; *p < 0.05, **p < 0.01, ***p < 0.001, and ****p < 0.0001 two-way ANOVA, followed by the Bonferroni post-test.

(I) Representative immunofluorescence staining of LTL (green) and PODXL (red) in kidney organoids cultured in the EGM and REGM media. Scale bar represents 400 μM (EGM) and 500 μM (REGM).

(J) Quantification of LTL positive cells in kidney organoids cultured in the EGM or REGM media. The y axis represents relative fluorescence. The data are presented as mean ±SEM. n = 3 organoids/group.

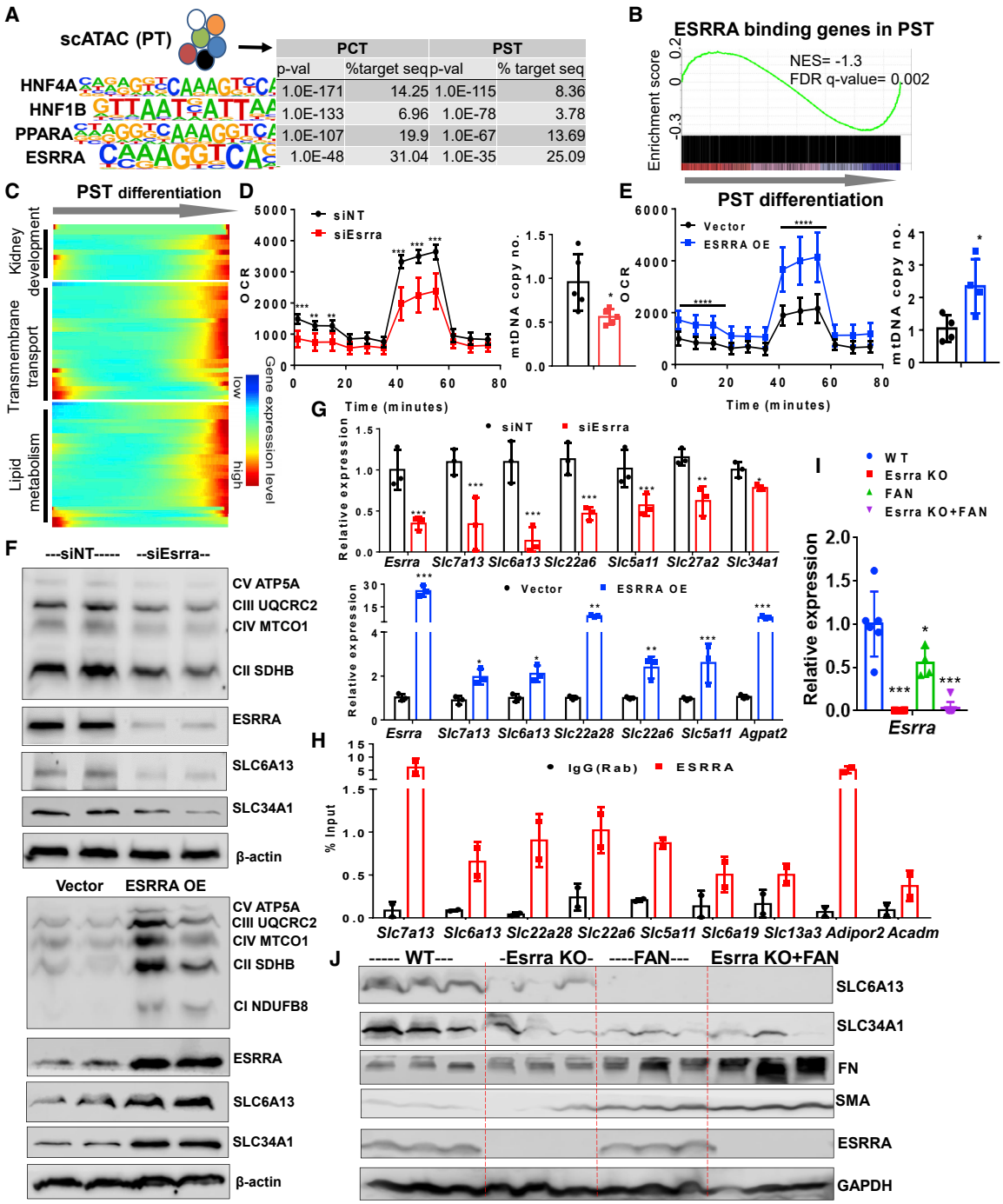

Figure 6. ESRRA Drives PT Differentiation State and Protects from Kidney Disease

(A) Top transcription factor-binding motifs significantly enriched in PT-cell-specific open chromatin regions that are identified from mouse single-cell ATAC-sequencing. p values and percentages of target sequences among all open chromatin regions are shown in the table on right.

(B) Gene set enrichment analysis (GSEA) enrichment plot of ESRRA target genes along with PST cell differentiation.

(C) Heatmap showing the expression changes of ESRRA target genes along the PST differentiation trajectory (ordered from Figure 4C) grouped by functional annotation (kidney development, transmembrane transport, and lipid metabolism).

(D) OCR (pmol/min/μg of protein) and mtDNA copy number (ratio of mtDNA to nuclear DNA) in LTL$^+$ PT cells transfected with non-target siRNA (siNT: black) and ESRRA siRNA (si*Esrra*: red) for 2 days. *p < 0.05, **p < 0.01, ***p < 0.001 versus siNT.

(E) OCR and mtDNA copy no. in LTL$^+$ PT cells transfected with vector alone (black) and ESRRA expressing vector (ESSRA OE: Blue) for 48 h. *p < 0.05, **p < 0.01, ***p < 0.001 versus vector.

(F) Protein levels of OXPHOS, ESRRA, SLC6A13, and SLC34A1 in LTL$^+$ PT cells transfected with si*Esrra* (upper panel) or ESRRA OE (lower panel) shown by Western blot. β-actin was used as a loading control.

(legend continued on next page)

Finally, we examined the expression of *ESRRA* and its target genes in 431 microdissected human kidneys (Table S7). The expression of *ESRRA* was lower in disease samples and strongly correlated with both eGFR and kidney fibrosis (Figure S7B). Protein expression of ESRRA was mostly localized to the nuclei of PTs, and it was markedly lower in human CKD samples (Figure S7C). The expression of *ESRRA* in human kidney tubule samples correlated with lipid metabolism and PT markers as well as with membrane transporter genes that are ESRRA targets (Figure 7D). These results confirm the relationship between the PT (differentiation) state and metabolism via ESRRA and PPARA.

DISCUSSION

Here, we present a comprehensive analysis using mouse scRNA and epigenome analysis, cultured cells, mouse models, patient samples, and kidney organoids to demonstrate that PT cells exist in different differentiation states in health and disease conditions. Our results highlight PT cellular metabolism as one of the main drivers of PT cell differentiation, identifying ESRRA as a central player in coupling metabolism and differentiation by directly binding and regulating the expression of PT genes. Furthermore, our observations describe how ESRRA together with HNF1B, HNF4A, and PPARA likely forms a complex network regulating PT metabolism and differentiation. ESRRA-driven PT metabolism and differentiation plays a critical role in protecting the kidney from injury and correlates with kidney disease severity in patient samples.

We show that the gene expression changes observed in bulk RNA-seq analysis mostly reflected cell heterogeneity of diseased mouse and human kidney samples. For example, PT-specific genes had lower expression levels in bulk RNA-seq analysis; however, many of these genes showed no clear change at a single-cell level. Genes that showed higher expression in disease samples were mostly genes exclusively expressed in immune cells; however, they did not show marked changes in the single-cell data when control and disease samples were compared. There was a marked increase in cell diversity of healthy and diseased samples, which mostly related to the increase in the diversity of immune cells.

We provide a high-resolution comprehensive analysis of cell-type-specific changes in two different mouse kidney fibrosis models. We identified different PT cell subtypes in healthy and disease states. In addition to the known PCT and PST segments, we also identified precursor-like cells. Cell heterogeneity was significantly higher in diseased PT cells as we identified proliferating cells, immune marker expressing cells and transitional cells (such as PCT and PST intermediate cells), and PT-LOH intermediate cells. Future studies will determine the role of these cells in disease development. It is important to note that these cell populations represented a continuum between the established PCT and PST cells rather than true discrete groups. Using trajectory and clustering methods, we identified cell state differences among PT cells. We identified precursor cells that expressed high levels of *Igfbp7* but lower levels of differentiated PT cell markers. IGFBP7 is one of the best-known biomarkers of AKI (Meersch et al., 2014; Vijayan et al., 2016). Further studies shall examine the connection between the kidney and urinary IGFBP7 expression, renal injury, and outcome.

We found that in diseased kidneys, fewer PT cells were in the terminal differentiation state. Increased death of differentiated cells could have contributed to this finding; however, only minimal changes in cell death were observed at the stages examined (Bielesz et al., 2010). Consistent with prior reports, Wingless-related integration site (Wnt) gene expression correlated with cell differentiation in one but not in the second kidney fibrosis model (Edeling et al., 2016; He et al., 2009; Kato et al., 2011; Rinkevich et al., 2014). Changes in lipid metabolism, FAO, and OXPHOS were consistent in both models. This might be consistent with earlier reports that such developmental pathways regulate metabolic changes in diseased kidneys (Huang et al., 2018). Overall, our results indicate that kidney PT cells exist in different states where higher expression of cell function genes (e.g., SLCs) strongly correlates with higher expression of FAO and OXPHOS genes.

Biologically, the coupling of metabolism and cell state makes perfect sense, as it harmoniously couples energy production and utilization with cellular function. Coupling of cell state and metabolism have been best demonstrated in the field of immunometabolism. For example, effector T cells exhibit high glycolysis, whereas regulatory cells have higher FAO and mTORC1 activation, which in turn drives effector differentiation while suppressing regulatory generation (Angelin et al., 2017; Delgoffe et al., 2009; Michalek et al., 2011). Dysregulated metabolism contributes to disease development, as T cells from systemic lupus erythematosus patients exhibit increased glycolysis and OXPHOS, whereas increased fatty acid biosynthesis and reduced ROS levels are associated with rheumatoid arthritis (Kornberg et al., 2018; Shen et al., 2017; Yang et al., 2013; Yin et al., 2015). Recently, sodium-glucose cotransporter 2 inhibitors have shown remarkable success in reducing the decline the kidney function (Barnett et al., 2014), therefore it is possible that reducing the PT cellular energy requirement is part of their mechanism of action.

Our results, for the first time, define the key role of several nuclear receptors such as PPARA and ESRRA in driving PT cell differentiation. ESRRA is a critical transcription factor that regulates mitochondrial biogenesis and FAO (Singh et al., 2018; Soriano et al., 2006). ESRRA remains an underappreciated nuclear receptor and metabolic target owing to its diverse role in multiple

(G) Relative mRNA levels of *Esrra* and variety of SLC markers (*Slc7a13, Slc6a13, Slc22a6, Slc5a11, Slc27a2*, and *Slc34a1*) in LTL+ PT cells transfected with siNT, *siEsrra* (red), and ESRRA OE plasmid (blue). *$p < 0.05$, **$p < 0.01$, ***$p < 0.001$ versus siNT/vector.

(H) ChIP-qPCR of ESRRA showed enrichment in genes including SLC markers (*Slc7a13, Slc6a13, Slc22a28, Slc5a11, Slc6a19*, and *Slc13a3*) and metabolic genes (*Adipor2* and *Acadm*) in LTL^+ PT cells compared with IgG control. The data are represented as mean ± SEM.

(I) Relative gene expression of *Esrra* measured by qRT-PCR in kidneys of wild-type (n = 4), Esrra KO mice (n = 6), and FA-treated wild-type mice (n = 4) or FA-treated Esrra KO mice (n = 8). *$p < 0.05$, **$p < 0.01$, and ***$p < 0.001$ versus wild-type.

(J) Protein levels of SLC6A13, SLC34A1, FN, SMA, and ESRRA in kidneys of wild-type, Esrra KO mice, and FA-injected or FA-treated Esrra KO mice were analyzed by western blot. GAPDH was used as a loading control.

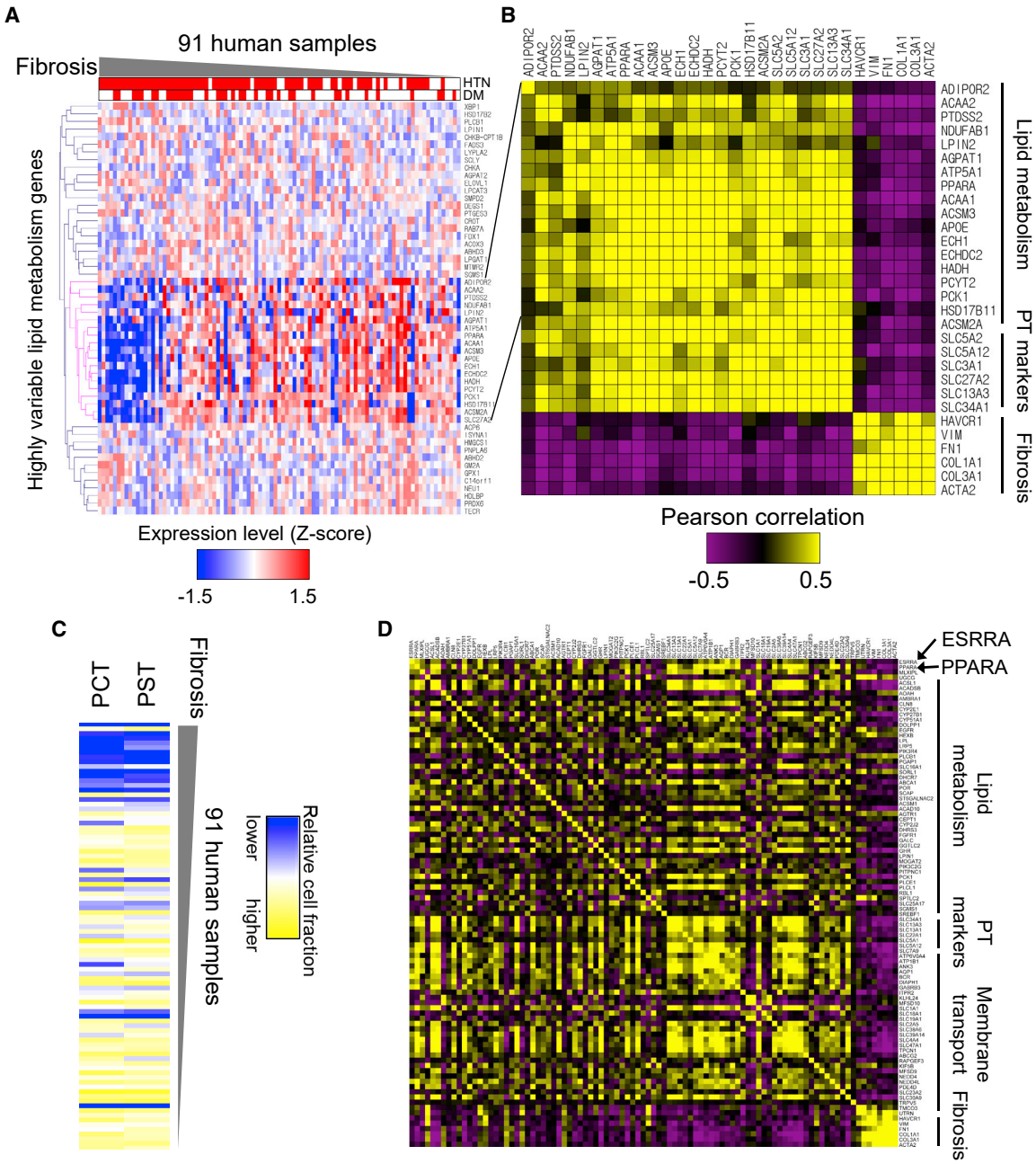

Figure 7. ESRRA-Driven Metabolic Changes Correlate with Kidney Disease Severity in Patient Samples

(A) relative expression levels of the highly variable lipid metabolism genes that were identified along the mouse PT cell differentiation trajectory (Figure 4) in 91 microdissected human tubules. The human kidney samples were ordered based on the degree of fibrosis.

(B) Heatmap showing Pearson's correlation coefficient between lipid metabolism genes, PT cell markers, and fibrosis markers in the human samples (yellow positive correlation, purple negative correlation, and intensity indicates the strength of correlation).

(C) Heatmap showing the relative cell fraction changes, calculated by *in silico* deconvolution (CellCODE) of the 91 human kidney RNA profiling data. The human kidney samples were ordered based on their fibrosis scores.

(D) Heatmap showing correlation coefficients between lipid metabolism genes, PT cell markers, and transmembrane transport genes that contain ESRRA binding motifs in their promoter or gene body and fibrosis markers in the human samples (yellow positive correlation, purple negative correlation, and intensity indicates the strength of correlation).

cellular signaling pathways and its function as a co-regulator of metabolism. Here, we show that ESRRA not only transcriptionally regulates mitochondrial and metabolic genes but also directly binds to genes associated with PT differentiation, such as a variety of SLCs. ESRRA target gene expression shows consistent changes in PT cell differentiation *in vivo* in mice and

in patients, thus supporting the key role of ESRRA in driving cell state. ESRRA overexpression improved not only metabolism and mitochondrial function but also PT differentiation, and its inhibition resulted in impaired FAO and OXPHOS with altered differentiation state. We found that other transcription factors such as ESRRG and PPARA levels increased in the absence of ESRRA, which might be responsible for the lack of phenotypic changes at baseline; however, this compensation was insufficient to protect *Esrra* KO mice during kidney injury (Zhao et al., 2018; Marable et al., 2020). Previous studies have also showed the role of *Esrrg* in kidney tubules (Zhao et al., 2018).

It has been difficult to induce PT cell differentiation in cultured organoids (Combes et al., 2019; Wu et al., 2018). Using human kidney organoids, we show that FAO and OXPHOS directly drive the differentiation of PT cells. Our data indicate that increasing the activity of *Esrra* (and *Ppara*) could be beneficial for PT cell differentiation not only in mouse model in vivo but also in cultured organoids in vitro.

In summary, we show the continuum of PT cell states in health and disease and the key role of metabolism in driving PT cell state. ESRRA couples cell differentiation state and metabolism by regulating not only the expression of cellular metabolism but also the expression of key cell-type-specific genes. The work provides new opportunities to manipulate cell fate, PT cell differentiation, and metabolism based on their reliance on nuclear receptors such as ESRRA.

Limitations of the Study

There are several limitations of our study, and future studies shall carefully examine changes observed in non-PT cells in the context of kidney fibrosis and in patients with kidney disease. Follow-up studies should examine the large number of genes and cell type changes identified by single-cell analysis. Future studies are needed to study the detailed ESRRA regulatory network in the kidney and its interaction with other key PT transcription factors such as PPARA, HNF1B, and HNF4A.

STAR★METHODS

Detailed methods are provided in the online version of this paper and include the following:

- KEY RESOURCES TABLE
- RESOURCE AVAILABILITY
  - Lead contact
  - Materials Availability
  - Data and Code Availability
- EXPERIMENTAL MODEL AND SUBJECT DETAILS
  - Mouse Models
  - Isolation and Culture of *LTL*$^+$ PT Cells
  - Kidney Organoids Differentiation
- METHOD DETAILS
  - Preparation of Single-Cell Suspension
  - Single-cell RNA Sequencing
  - Alignment and Generation of Data Matrix
  - Data Quality Control, Preprocessing and Dimension Reduction
  - Removal of Doublet-like Cells
  - Cell Clustering Analysis
  - Mouse Bulk RNA-sequencing Analysis
  - Estimation of Cell Proportions
  - Identification of Marker Genes and Differentially Expressed Genes
  - Cell Trajectory Analysis
  - Monocle2
  - Single Cell ATAC Sequencing Analysis
  - Human Bulk Gene Profiling Data Analysis
  - Single Cell Suspension from Kidney organoid
  - Mitotracker Green FM Flow Cytometric Analysis
  - Protein Extraction and Western Blot Analysis in Kidney Organoids
  - Immunofluorescence
  - Mitochondrial DNA Analysis
  - PT Cell Transfection
  - Oxygen Consumption Rate (OCR)
  - Chromatin Immunoprecipitation qPCR
  - Fenofibrate Treatment
  - XCT790 Treatment
  - qRT-PCR
  - Western Blot
  - Histological Analysis
- QUANTIFICATION AND STATISTICAL ANALYSIS
  - Data Representation and Statistical Analysis

SUPPLEMENTAL INFORMATION

Supplemental Information can be found online at https://doi.org/10.1016/j.cmet.2020.11.011.

ACKNOWLEDGMENTS

Work in the Susztak lab is supported by NIH National Institute of Diabetes and Digestive and Kidney Diseases grants R01DK076077, R01 DK087635, and DP3 DK108220. We thank the University of Pennsylvania Diabetes Research Center (DRC) for the use of the Core services (P30-DK19525). J.P. is supported by the National Research Foundation of Korea funded by the Korea government (MSIP) (2019R1C1C1005403 and 2019R1A4A1028802). J.Z. and L.P. are supported by the Office of the Assistant Secretary of Defense for Health Affairs through the Peer-Reviewed Medical Research Program under award W81XWH-16-1-0400, NIH DK111495, and pilot awards from the Diabetes Research Center at the University of Pennsylvania NIH DK19525. M.S.B. is supported by German Research Foundation grant BA 6205/2-1. This work has received funding from the European Research Council (ERC) under the European Union's Horizon 2020 research and innovation Programme (StG-2014-640525_REGMAMKID to P.P. and N.M.). N.M. is also supported by the Spanish Ministry of Economy and Competitiveness/FEDER (SAF2017-89782-R), the Generalitat de Catalunya and CERCA Programme (2017 SGR 1306), Asociación Española contra el Cáncer (LABAE16006), and Institute of Health Carlos III (ACE2ORG). C.H.P. is supported by Marie Skłodowska-Curie Individual Fellowships (IF) grant agreement no. 796590. We thank Vincent Giguère (McGill University) for sharing the *Esrra* KO mice. N.M and C.H.P are supported by EFSD/Boehringer Ingelheim European Research Programme in Microvascular Complications of Diabetes. This work was supported in part by the ISCIII and FEDER through TERCEL RETIC RD16/0011/0005 and RD16/0011/0027. P.J.D. was supported by an American Heart Association postdoctoral fellowship (20POST35210738).

AUTHOR CONTRIBUTIONS

K.S., J.P., P.D., and N.M. conceived and led this study. J.P. performed all the single-cell data analysis. P.D., S.H., and R.S. performed animal studies. P.D. performed all cell culture experiments. P.D. and S.H. performed histological analysis. C.H.d.P. and P.P. performed organoid studies. T.D. and R.S.

performed kidney functional assay. S.Y.H., J.P.R., and F.P. contributed to organoid data analysis. J.P. performed computation analysis and helped by S.C., M.B., H.L., and X.S. P.J.D., H.M.K., K.B., M.L., L.P., and J.K. helped with data analysis. J.P., P.D., N.M., and K.S. wrote the paper.

DECLARATION OF INTERESTS

The Susztak lab is supported by Boehringer Ingelheim, Lilly, Regeneron, GSK, Merck, Bayer, and Gilead for work that is not related to the current manuscript.

Received: February 25, 2020
Revised: August 28, 2020
Accepted: November 12, 2020
Published: December 9, 2020

REFERENCES

Angelin, A., Gil-de-Gómez, L., Dahiya, S., Jiao, J., Guo, L., Levine, M.H., Wang, Z., Quinn, W.J., 3rd, Kopinski, P.K., Wang, L., et al. (2017). Foxp3 reprograms T cell metabolism to function in low-glucose, high-lactate environments. Cell Metab. *25*, 1282–1293.e7.

Angelotti, M.L., Ronconi, E., Ballerini, L., Peired, A., Mazzinghi, B., Sagrinati, C., Parente, E., Gacci, M., Carini, M., Rotondi, M., et al. (2012). Characterization of renal progenitors committed toward tubular lineage and their regenerative potential in renal tubular injury. Stem Cells *30*, 1714–1725.

Barnett, A.H., Mithal, A., Manassie, J., Jones, R., Rattunde, H., Woerle, H.J., Broedl, U.C., and EMPA-REG RENAL trial investigators. (2014). Efficacy and safety of empagliflozin added to existing antidiabetes treatment in patients with type 2 diabetes and chronic kidney disease: a randomised, double-blind, placebo-controlled trial. Lancet Diabetes Endocrinol. *2*, 369–384.

Beckerman, P., Qiu, C., Park, J., Ledo, N., Ko, Y.A., Park, A.D., Han, S.Y., Choi, P., Palmer, M., and Susztak, K. (2017). Human kidney tubule-specific gene expression based dissection of chronic kidney disease traits. EBioMedicine *24*, 267–276.

Bielesz, B., Sirin, Y., Si, H., Niranjan, T., Gruenwald, A., Ahn, S., Kato, H., Pullman, J., Gessler, M., Haase, V.H., and Susztak, K. (2010). Epithelial Notch signaling regulates interstitial fibrosis development in the kidneys of mice and humans. J. Clin. Invest. *120*, 4040–4054.

Breyer, M.D., and Susztak, K. (2016). The next generation of therapeutics for chronic kidney disease. Nat. Rev. Drug Discov. *15*, 568–588.

Cao, J., Cusanovich, D.A., Ramani, V., Aghamirzaie, D., Pliner, H.A., Hill, A.J., Daza, R.M., McFaline-Figueroa, J.L., Packer, J.S., Christiansen, L., et al. (2018). Joint profiling of chromatin accessibility and gene expression in thousands of single cells. Science *361*, 1380–1385.

Chang-Panesso, M., and Humphreys, B.D. (2017). Cellular plasticity in kidney injury and repair. Nat. Rev. Nephrol. *13*, 39–46.

Chikina, M., Zaslavsky, E., and Sealfon, S.C. (2015). CellCODE: a robust latent variable approach to differential expression analysis for heterogeneous cell populations. Bioinformatics *31*, 1584–1591.

Chung, K.W., Dhillon, P., Huang, S., Sheng, X., Shrestha, R., Qiu, C., Kaufman, B.A., Park, J., Pei, L., Baur, J., et al. (2019). Mitochondrial damage and activation of the STING pathway lead to renal inflammation and fibrosis. Cell Metab. *30*, 784–799.e5.

Combes, A.N., Zappia, L., Er, P.X., Oshlack, A., and Little, M.H. (2019). Single-cell analysis reveals congruence between kidney organoids and human fetal kidney. Genome Med *11*, 3.

de Lau, W., Barker, N., Low, T.Y., Koo, B.K., Li, V.S., Teunissen, H., Kujala, P., Haegebarth, A., Peters, P.J., van de Wetering, M., et al. (2011). Lgr5 homologues associate with Wnt receptors and mediate R-spondin signalling. Nature *476*, 293–297.

Delgoffe, G.M., Kole, T.P., Zheng, Y., Zarek, P.E., Matthews, K.L., Xiao, B., Worley, P.F., Kozma, S.C., and Powell, J.D. (2009). The mTOR kinase differentially regulates effector and regulatory T cell lineage commitment. Immunity *30*, 832–844.

Edeling, M., Ragi, G., Huang, S., Pavenstädt, H., and Susztak, K. (2016). Developmental signalling pathways in renal fibrosis: the roles of Notch, Wnt and Hedgehog. Nat. Rev. Nephrol. *12*, 426–439.

Garreta, E., Prado, P., Tarantino, C., Oria, R., Fanlo, L., Martí, E., Zalvidea, D., Trepat, X., Roca-Cusachs, P., Gavaldà-Navarro, A., et al. (2019). Fine tuning the extracellular environment accelerates the derivation of kidney organoids from human pluripotent stem cells. Nat. Mater. *18*, 397–405.

Gomez, I.G., MacKenna, D.A., Johnson, B.G., Kaimal, V., Roach, A.M., Ren, S., Nakagawa, N., Xin, C., Newitt, R., Pandya, S., et al. (2015). Anti-microRNA-21 oligonucleotides prevent Alport nephropathy progression by stimulating metabolic pathways. J. Clin. Invest. *125*, 141–156.

Grande, M.T., Sánchez-Laorden, B., López-Blau, C., De Frutos, C.A., Boutet, A., Arévalo, M., Rowe, R.G., Weiss, S.J., López-Novoa, J.M., and Nieto, M.A. (2015). Snail1-induced partial epithelial-to-mesenchymal transition drives renal fibrosis in mice and can be targeted to reverse established disease. Nat. Med. *21*, 989–997.

He, W., Dai, C., Li, Y., Zeng, G., Monga, S.P., and Liu, Y. (2009). Wnt/beta-catenin signaling promotes renal interstitial fibrosis. J. Am. Soc. Nephrol. *20*, 765–776.

Hellwege, J.N., Velez Edwards, D.R., Giri, A., Qiu, C., Park, J., Torstenson, E.S., Keaton, J.M., Wilson, O.D., Robinson-Cohen, C., Chung, C.P., et al. (2019). Mapping eGFR loci to the renal transcriptome and phenome in the VA Million Veteran program. Nat. Commun. *10*, 3842.

Huang, S., Park, J., Qiu, C., Chung, K.W., Li, S.Y., Sirin, Y., Han, S.H., Taylor, V., Zimber-Strobl, U., and Susztak, K. (2018). Jagged1/Notch2 controls kidney fibrosis via Tfam-mediated metabolic reprogramming. PLoS Biol. *16*, e2005233.

Kang, H.M., Ahn, S.H., Choi, P., Ko, Y.A., Han, S.H., Chinga, F., Park, A.S., Tao, J., Sharma, K., Pullman, J., et al. (2015). Defective fatty acid oxidation in renal tubular epithelial cells has a key role in kidney fibrosis development. Nat. Med. *21*, 37–46.

Kang, H.M., Huang, S., Reidy, K., Han, S.H., Chinga, F., and Susztak, K. (2016). Sox9-positive progenitor cells play a key role in renal tubule epithelial regeneration in mice. Cell Rep. *14*, 861–871.

Kato, H., Gruenwald, A., Suh, J.H., Miner, J.H., Barisoni-Thomas, L., Taketo, M.M., Faul, C., Millar, S.E., Holzman, L.B., and Susztak, K. (2011). Wnt/beta-catenin pathway in podocytes integrates cell adhesion, differentiation, and survival. J. Biol. Chem. *286*, 26003–26015.

Kornberg, M.D., Bhargava, P., Kim, P.M., Putluri, V., Snowman, A.M., Putluri, N., Calabresi, P.A., and Snyder, S.H. (2018). Dimethyl fumarate targets GAPDH and aerobic glycolysis to modulate immunity. Science *360*, 449–453.

Kovesdy, C.P., Bleyer, A.J., Molnar, M.Z., Ma, J.Z., Sim, J.J., Cushman, W.C., Quarles, L.D., and Kalantar-Zadeh, K. (2013). Blood pressure and mortality in U.S. veterans with chronic kidney disease: a cohort study. Ann. Intern. Med. *159*, 233–242.

La Manno, G., Soldatov, R., Zeisel, A., Braun, E., Hochgerner, H., Petukhov, V., Lidschreiber, K., Kastriti, M.E., Lönnerberg, P., Furlan, A., et al. (2018). RNA velocity of single cells. Nature *560*, 494–498.

Lake, B.B., Chen, S., Hoshi, M., Plongthongkum, N., Salamon, D., Knoten, A., Vijayan, A., Venkatesh, R., Kim, E.H., Gao, D., et al. (2019). A single-nucleus RNA-sequencing pipeline to decipher the molecular anatomy and pathophysiology of human kidneys. Nat. Commun. *10*, 2832.

Levin, A., Tonelli, M., Bonventre, J., Coresh, J., Donner, J.A., Fogo, A.B., Fox, C.S., Gansevoort, R.T., Heerspink, H.J.L., Jardine, M., et al. (2017). Global kidney health 2017 and beyond: a roadmap for closing gaps in care, research, and policy. Lancet *390*, 1888–1917.

Li, Y., Wen, X., and Liu, Y. (2012). Tubular cell dedifferentiation and peritubular inflammation are coupled by the transcription regulator Id1 in renal fibrogenesis. Kidney Int. *81*, 880–891.

Liu, J., Krautzberger, A.M., Sui, S.H., Hofmann, O.M., Chen, Y., Baetscher, M., Grgic, I., Kumar, S., Humphreys, B.D., Hide, W.A., and McMahon, A.P. (2014). Cell-specific translational profiling in acute kidney injury. J. Clin. Invest. *124*, 1242–1254.

Lovisa, S., LeBleu, V.S., Tampe, B., Sugimoto, H., Vadnagara, K., Carstens, J.L., Wu, C.C., Hagos, Y., Burckhardt, B.C., Pentcheva-Hoang, T., et al. (2015). Epithelial-to-mesenchymal transition induces cell cycle arrest and parenchymal damage in renal fibrosis. Nat. Med. *21*, 998–1009.

Maekawa, H., Inoue, T., Ouchi, H., Jao, T.M., Inoue, R., Nishi, H., Fujii, R., Ishidate, F., Tanaka, T., Tanaka, Y., et al. (2019). Mitochondrial damage causes inflammation via cGAS-STING signaling in acute kidney injury. Cell Rep. *29*, 1261–1273.e6.

Marable, S.S., Chung, E., and Park, J. (2020). Hnf4a is required for the development of Cdh6-expressing progenitors into proximal tubules in the mouse kidney. bioRxiv. https://doi.org/10.1101/2020.02.16.951731.

McGinnis, C.S., Murrow, L.M., and Gartner, Z.J. (2019). DoubletFinder: doublet detection in single-cell RNA sequencing data using artificial nearest neighbors. Cell Syst. *8*, 329–337.e4.

Meersch, M., Schmidt, C., Van Aken, H., Martens, S., Rossaint, J., Singbartl, K., Görlich, D., Kellum, J.A., and Zarbock, A. (2014). Urinary TIMP-2 and IGFBP7 as early biomarkers of acute kidney injury and renal recovery following cardiac surgery. PLoS One *9*, e93460.

Menon, R., Otto, E.A., Hoover, P., Eddy, S., Mariani, L., Godfrey, B., Berthier, C.C., Eichinger, F., Subramanian, L., Harder, J., et al. (2020). Single cell transcriptomics identifies focal segmental glomerulosclerosis remission endothelial biomarker. JCI Insight *5*, e133267.

Michalek, R.D., Gerriets, V.A., Jacobs, S.R., Macintyre, A.N., MacIver, N.J., Mason, E.F., Sullivan, S.A., Nichols, A.G., and Rathmell, J.C. (2011). Cutting edge: distinct glycolytic and lipid oxidative metabolic programs are essential for effector and regulatory CD4+ T cell subsets. J. Immunol. *186*, 3299–3303.

Park, J., Shrestha, R., Qiu, C., Kondo, A., Huang, S., Werth, M., Li, M., Barasch, J., and Suszták, K. (2018). Single-cell transcriptomics of the mouse kidney reveals potential cellular targets of kidney disease. Science *360*, 758–763.

Qiu, C., Huang, S., Park, J., Park, Y., Ko, Y.-A., Seasock, M.J., Bryer, J.S., Xu, X.X., Song, W.C., Palmer, M., et al. (2018). Renal compartment-specific genetic variation analyses identify new pathways in chronic kidney disease. Nat. Med. *24*, 1721–1731.

Quiros, P.M., Goyal, A., Jha, P., and Auwerx, J. (2017). Analysis of mtDNA/nDNA ratio in mice. Curr. Protoc. Mouse Biol. *7*, 47–54.

Reidy, K., Kang, H.M., Hostetter, T., and Susztak, K. (2014). Molecular mechanisms of diabetic kidney disease. J. Clin. Invest. *124*, 2333–2340.

Rinkevich, Y., Montoro, D.T., Contreras-Trujillo, H., Harari-Steinberg, O., Newman, A.M., Tsai, J.M., Lim, X., Van-Amerongen, R., Bowman, A., Januszyk, M., et al. (2014). In vivo clonal analysis reveals lineage-restricted progenitor characteristics in mammalian kidney development, maintenance, and regeneration. Cell Rep. *7*, 1270–1283.

Shen, Y., Wen, Z., Li, Y., Matteson, E.L., Hong, J., Goronzy, J.J., and Weyand, C.M. (2017). Metabolic control of the scaffold protein TKS5 in tissue-invasive, proinflammatory T cells. Nat. Immunol. *18*, 1025–1034.

Singh, B.K., Sinha, R.A., Tripathi, M., Mendoza, A., Ohba, K., Sy, J.A.C., Xie, S.Y., Zhou, J., Ho, J.P., Chang, C.-Y., et al. (2018). Thyroid hormone receptor and ERRα coordinately regulate mitochondrial fission, mitophagy, biogenesis, and function. Sci. Signal. *11*, eaam5855.

Smillie, C.S., Biton, M., Ordovas-Montanes, J., Sullivan, K.M., Burgin, G., Graham, D.B., Herbst, R.H., Rogel, N., Slyper, M., Waldman, J., et al. (2019). Intra- and inter-cellular rewiring of the human colon during ulcerative colitis. Cell *178*, 714–730.e22.

Soriano, F.X., Liesa, M., Bach, D., Chan, D.C., Palacín, M., and Zorzano, A. (2006). Evidence for a mitochondrial regulatory pathway defined by peroxisome proliferator-activated receptor-gamma coactivator-1 alpha, estrogen-related receptor-alpha, and mitofusin 2. Diabetes *55*, 1783–1791.

Tran, M., Tam, D., Bardia, A., Bhasin, M., Rowe, G.C., Kher, A., Zsengeller, Z.K., Akhavan-Sharif, M.R., Khankin, E.V., Saintgeniez, M., et al. (2011). PGC-1alpha promotes recovery after acute kidney injury during systemic inflammation in mice. J. Clin. Invest. *121*, 4003–4014.

Tran, M.T., Zsengeller, Z.K., Berg, A.H., Khankin, E.V., Bhasin, M.K., Kim, W., Clish, C.B., Stillman, I.E., Karumanchi, S.A., Rhee, E.P., and Parikh, S.M. (2016). PGC1α drives NAD biosynthesis linking oxidative metabolism to renal protection. Nature *531*, 528–532.

Trapnell, C., Cacchiarelli, D., Grimsby, J., Pokharel, P., Li, S., Morse, M., Lennon, N.J., Livak, K.J., Mikkelsen, T.S., and Rinn, J.L. (2014). The dynamics and regulators of cell fate decisions are revealed by pseudotemporal ordering of single cells. Nat. Biotechnol. *32*, 381–386.

Vijayan, A., Faubel, S., Askenazi, D.J., Cerda, J., Fissell, W.H., Heung, M., Humphreys, B.D., Koyner, J.L., Liu, K.D., Mour, G., et al. (2016). Clinical use of the urine biomarker [TIMP-2] × [IGFBP7] for acute kidney injury risk assessment. Am. J. Kidney Dis. *68*, 19–28.

Woroniecka, K.I., Park, A.S., Mohtat, D., Thomas, D.B., Pullman, J.M., and Susztak, K. (2011). Transcriptome analysis of human diabetic kidney disease. Diabetes *60*, 2354–2369.

Wu, H., Kirita, Y., Donnelly, E.L., and Humphreys, B.D. (2019). Advantages of single-nucleus over single-cell RNA sequencing of adult kidney: rare cell types and novel cell states revealed in fibrosis. J. Am. Soc. Nephrol. *30*, 23–32.

Wu, H., Uchimura, K., Donnelly, E.L., Kirita, Y., Morris, S.A., and Humphreys, B.D. (2018). Comparative analysis and refinement of human PSC-derived kidney organoid differentiation with single-cell transcriptomics. Cell Stem Cell *23*, 869–881.e8.

Wuttke, M., Li, Y., Li, M., Sieber, K.B., Feitosa, M.F., Gorski, M., Tin, A., Wang, L., Chu, A.Y., Hoppmann, A., et al. (2019). A catalog of genetic loci associated with kidney function from analyses of a million individuals. Nat. Genet. *51*, 957–972.

Yang, Z., Fujii, H., Mohan, S.V., Goronzy, J.J., and Weyand, C.M. (2013). Phosphofructokinase deficiency impairs ATP generation, autophagy, and redox balance in rheumatoid arthritis T cells. J. Exp. Med. *210*, 2119–2134.

Yin, Y., Choi, S.C., Xu, Z., Perry, D.J., Seay, H., Croker, B.P., Sobel, E.S., Brusko, T.M., and Morel, L. (2015). Normalization of CD4+ T cell metabolism reverses lupus. Sci. Transl. Med. *7*, 274ra18.

Young, M.D., Mitchell, T.J., Vieira Braga, F.A., Tran, M.G.B., Stewart, B.J., Ferdinand, J.R., Collord, G., Botting, R.A., Popescu, D.M., Loudon, K.W., et al. (2018). Single-cell transcriptomes from human kidneys reveal the cellular identity of renal tumors. Science *361*, 594–599.

Zeisberg, M., and Duffield, J.S. (2010). Resolved: EMT produces fibroblasts in the kidney. J. Am. Soc. Nephrol. *21*, 1247–1253.

Zhang, R., Boareto, M., Engler, A., Louvi, A., Giachino, C., Iber, D., and Taylor, V. (2019). Id4 downstream of Notch2 maintains neural stem cell quiescence in the adult hippocampus. Cell Rep. *28*, 1485–1498.e6.

Zhao, J., Lupino, K., Wilkins, B.J., Qiu, C., Liu, J., Omura, Y., Allred, A.L., McDonald, C., Susztak, K., Barish, G.D., and Pei, L. (2018). Genomic integration of ERRgamma-HNF1beta regulates renal bioenergetics and prevents chronic kidney disease. Proc. Natl. Acad. Sci. USA *115*, E4910–E4919.

Zheng, M., Cai, J., Liu, Z., Shu, S., Wang, Y., Tang, C., and Dong, Z. (2019). Nicotinamide reduces renal interstitial fibrosis by suppressing tubular injury and inflammation. J. Cell. Mol. Med. *23*, 3995–4004.

STAR★METHODS

KEY RESOURCES TABLE

REAGENT or RESOURCE	SOURCE	IDENTIFIER
Antibodies		
Primary antibodies for Immunoblots		
Anti-COX IV antibody	Abcam	Cat# ab16056; RRID: AB_443304
Total OXPHOS Rodent WB Antibody Cocktail	Abcam	Cat# ab110413; RRID: AB_2629281
GAPDH	CST(14C10)	Cat# 2118; RRID: AB_561053
PGC1a	Calbiochem	Cat#KP9803
SLC6A13	Invitrogen	Cat# PA5-68331; RRID: AB_2691971
α-Tubulin	Sigma	Cat# T9026; RRID: AB_477593
SMA	Sigma	Cat# A5228; RRID: AB_262054
FN	Abcam	Cat# ab2413; RRID: AB_2262874
ESRRA	CST	Cat# 13826; RRID: AB_2750873
β-actin	Millipore	Cat# A3854; RRID: AB_262011
Secondary antibodies for Immunoblots		
Anti-mouse IgG, HRP-linked Antibody	CST	Cat# 7076; RRID: AB_330924
Anti-rabbit IgG, HRP-linked Antibody	CST	Cat# 7074; RRID: AB_2099233
Antibodies for Immunohistochemistry (IHC)		
ESRRA	CST	Cat# 13826; RRID: AB_2750873
SLC34A1	Novus Biologicals	Cat# NBP2-42216; RRID: AB_2801654
SLC7A13	Creative Diagnostics	Cat# CPBT-45312RH; RRID: AB_2378853
SLC6A13	Invitrogen	Cat# PA5-68331; RRID: AB_2691971
Antibodies for Immunofluorescence (IF)		
LTL	Vector laboratories	Cat# FL-1321; RRID: AB_2336559
PODXL	Thermofischer	Cat# 39-3800; RRID: AB_2533411
IRDye®680RD	LI-COR	Cat# 926-68070; RRID: AB_10956588
Ki67	CST	Cat# 12202; RRID: AB_2620142
A555	Life technology	Cat# A-31572; RRID: AB_162543
Antibodies for FACS		
LTL	Vector laboratories	Cat# B-1325; RRID: AB_2336558
Biological Samples		
Human kidney samples	Chung et al., 2019	N/A
Chemicals, Peptides, and Recombinant Proteins		
MitoTracker Green	Life Technology	Cat#M7514
Collagenase IV	Life Technologies	Cat#17104019
Trypan blue solution	Sigma	Cat#T8154
Protease inhibitor cocktail	Roche	Cat#11836153001
EDTA solution	Life Technologies	Cat#15575-038
Accumax	Stem Cell Technologies	Cat#07921
Phosphate buffered saline (PBS) pH 7.4 (1x)	Life Technologies	Cat#1001–015
Essential 8 medium	Life Technologies	Cat#A1517001
Vitronectin	Life Technologies	Cat#A14700
Fenofibrate	Sigma	CAS#49562-28-9
RPMI 1640	Gibco	Cat#21875-034
EGM media	Lonza	Cat#CC-3162
REGM media	Lonza	Cat#CC-4127
RIPA buffer	Cell signaling	Cat#9806

(*Continued on next page*)

Continued

REAGENT or RESOURCE	SOURCE	IDENTIFIER
SYBR Green PCR Master Mix	Applied Biosystem	Cat#KK4605
Fluoromount-G	Southern Biotech	Cat# 0100-01
XCT790	Tocris	Cat#3928
Folic Acid	Fisher Scientific	Cat#AC216630500
Lipofectamine 3000	ThermoFisher	Cat#11668027
CHIR99021	Merck	Cat#SML1046; CAS: 252917-06-9
Recombinant human FGF9	PeproTech	Cat#100-23
Heparin	Merck	Cat#H3149; CAS: 9041-08-1
Activin A	Vitro	Cat#338-AC-050
Dimethyl Sulfoxide (DMSO)	Merck	Cat#D2650; CAS: 67-68-5
Cell culture grade distilled water	Life Technologies	Cat#15230-089
Paraformaldehyde solution 4% in PBS	Santa Cruz	Cat#sc-281692
Hoechst	Molecular probes	Cat# H-1399
Critical Commercial Assays		
BCA Protein Assay Kit	Thermo Scientific	Cat#23225
Multi Tissue dissociation kit	Miltenyi	Cat#130-110-201
Anti-Biotin microbeads	Miltenyi	Cat#130-090-485
cDNA Reverse Transcription Kit	Applied Biosystems	Cat#4368813
Rneasy Mini Kit	Qiagen	Cat#74106
MAGnify™ ChIP Kit	Thermo Scientific	Cat# 492024
DNeasy Blood & Tissue Kits	Qiagen	Cat#69506
Seahorse XF Cell Mito Stress Test kit	Agilent Technologies	Cat#103708-100
Seahorse XFe96 FluxPak mini	Agilent Technologies	Cat#102601-100
VECTASTAIN® Elite ABC-HRP Kit	Vector laboratories	Cat# PK-6100
Streptavidin/Biotin blocking kit	Vector laboratories	Cat#SP-2002
Deposited Data		
scATAC seq data	(Cao et al., 2018)	GSE117089
scRNA-seq of FAN kidneys of mice	GEO	GSE156686
scRNA seq data kidney organoids	GEO	GSE152765
Experimental Models: Organisms/Strains		
ESRRA Knock-out	Dr. Vincent Giguère Research Lab	McGill University
Oligonucleotides		
Primers for qPCR, mtDNA copy no., and ChIP-qPCR, see Table S6	This paper	N/A
Recombinant DNA		
pAd-track-Esrra	Dr. Liming Pei lab	University of Pennsylvania
pcDNA3.1-Ppara	Dr. Liming Pei lab	University of Pennsylvania
pc-DNA3.1-HNF1B	Dr. Liming Pei lab	University of Pennsylvania
pAd-track-HNF4A	Dr. Liming Pei lab	University of Pennsylvania
Experimental Models: Cell Lines		
ES[4] Human Embryonic Stem Cell line	The National Bank of Stem Cells (ISCIII,Madrid)	https://www.isciii.es/
Software and Algorithms		
ImageJ	NIH	https://imagej.nih.gov/ij
Prism 5	Graphpad Software	https://www.graphpad.com/scientific-software/prism
Image Studio Lite Version 5.2 software	LICOR	https://www.licor.com/bio/image-studio-lite/d5
FlowJo Software	FlowJo	N/A

(*Continued on next page*)

Continued

REAGENT or RESOURCE	SOURCE	IDENTIFIER
Cell Ranger 2.0	10x Genomics	https://support.10xgenomics.com/single-cell-gene-expression/software/downloads/latest
Seurat R package 2.3.4	open source	https://satijalab.org/seurat/
DoubletFinder	open source	https://github.com/chris-mcginnis-ucsf/DoubletFinder
STAR-2.4.1d	open source	https://github.com/alexdobin/STAR
HTSeq-0.6.1	open source	https://htseq.readthedocs.io/en/release_0.11.1/history.html#version-0-6-1
DESeq2 1.10.1	open source	https://bioconductor.org/packages/release/bioc/html/DESeq2.html
CellCODE	open source	https://github.com/mchikina/CellCODE/
Velocyto	open source	https://github.com/velocyto-team/velocyto.R
Monocle2 2.4.0	open source	http://cole-trapnell-lab.github.io/monocle-release/

RESOURCE AVAILABILITY

Lead contact

Further information and requests for resources and reagents should be directed to and will be fulfilled by the lead contact: Katalin Susztak. Email: ksusztak@pennmedicine.upenn.edu

Materials Availability

This study did not generate new unique reagents.

Data and Code Availability

The accession number for the scRNA-seq data reported in this paper are NCBI GEO: GSE156686 and GSE152765. All other data are available upon reasonable request for corresponding author. Furthermore, the data is available via an interactive web browser at http://susztaklab.com/VisCello/.

EXPERIMENTAL MODEL AND SUBJECT DETAILS

Mouse Models

Animal studies were approved by the Institutional Animal Care and Use Committee (IACUC) of the University of Pennsylvania. Mice were housed in the Institute pathogen free animal house (12 h dark/light cycle) in a temperature- and humidity-controlled environment (23 ± 1°C) and fed with standard mouse diet and water ad libitum. 5- to 8-week-old male C57BL/6 wild type mice were used in the study. *Esrra* KO mice were kindly provided by Dr. Liming Pei (University of Pennsylvania) and littermates were used from in-house matings. All animals were pathogen free and healthy prior to the beginning of experiments. For all the mice experiments, mice were randomly assigned to experimental groups, unless stated otherwise.

For fenofibrate experiment, the PPARA agonist fenofibrate (50 mg/kg for 3 days and 100 mg/kg for 5 days) was administered by oral gavage starting one day before the folic acid (FA) injection. Mice were injected with FA (250 mg/kg once, dissolved in 300 mM $NaHCO_3$) intraperitoneally and sacrificed on day 7. For the unilateral ureteral obstruction (UUO) model, mice underwent ligation of the left ureter and were sacrificed on day 7.

Isolation and Culture of *LTL*$^+$ PT Cells

Primary mouse proximal tubule epithelial cells were isolated from kidneys of 4 weeks old wild type mice and LTL$^+$ cells fractions were purified from single cell suspension of PT cells by using biotinylated lotus tetragonolobus lectin antibody (LTL) (L-132; Vector Laboratories) and anti-biotin microbeads (MACS Miltenyi Biotec). LTL$^+$ cells were grown in primary cell culture media (RPMI 1640 supplemented with 10% FBS, 20 ng ml^{-1} EGF, 20 ng ml^{-1} bFGF and 1% penicillin-streptomycin).

Kidney Organoids Differentiation

ES[4] human embryonic stem cells were grown on vitronectin coated plates (1001-015, Life Technologies). Cells were incubated in 0.5mM EDTA (Merck) at 37°C for 3 minutes for disaggregation. To avoid the separation of the stem cell clusters, cells were then carefully collected into 12 ml supplemented Essential 8 Basal medium. For cell counting, 1 mL cell suspension was centrifuged for 4 minutes at 400 g and the pellet was resuspended in 200 μl of AccumaxTM (StemCell Technologies) to obtain single cells. Cells were incubated in AccumaxTM at 37°C for 3 minutes and next, 800 μL of FBS were added to stop the disaggregation. After cell counting (Countess ® Automated Cell Counter), 100,000 cells/well were plated on a 24 multi-well plate coated with 5μl/ml vitronectin. Cells

were incubated in supplemented Essential 8 Basal medium at 37°C overnight. The next day (day 0), the differentiation was initiated by treating the cells with 8 μM CHIR (Merck) in Advanced RPMI 1640 basal medium (ThermoFisher) supplemented with 1% Penicillin-Streptomycin and 1% of GlutaMAXTM (ThermoFisher) for 3 days and changing the medium every day. On day 3, CHIR treatment was removed and cells were cultured in 200 ng·ml^{-1} FGF9 (Peprotech), 1 μg·ml^{-1} heparin (Merck) and 10 ng·ml-1 activin A (Act A) (Vitro) in supplemented Advanced RPMI for 1 day. On day 4, spheroid organoids were generated. Cells were rinsed twice with PBS, collected using supplemented Advanced RPMI and plated at 100,000 cells/well on a V-shape 96 multi-well plate. They were treated with 5 μM CHIR, 200ng·ml-1 FGF9 and 1 μg·ml-1 Heparin in supplemented Advanced RPMI. Organoids were incubated for 1 hour at 37°C, CHIR induction was removed and they were incubated in 200 ng·ml-1 FGF9 and 1 μg·ml-1 Heparin in supplemented Advanced RPMI for 7 days with medium change every other day. From day 11, factors were eliminated, and cells were incubated only in supplemented Advanced RPMI for 5 days, medium was changed every other day.

METHOD DETAILS

Preparation of Single-Cell Suspension

Euthanized mice were perfused with chilled 1x PBS via the left ventricle. Kidneys were harvested, minced into approximately 1 mm^3 cubes and digested using Multi Tissue dissociation kit (Miltenyi, 130-110-201). The tissue was homogenized using 21G and 26 1/2G syringes. Up to 0.25 g of the tissue was digested with 50ul of Enzyme D, 25 ul of Enzyme R and 6.75 μl of Enzyme A in 1 ml of RPMI and incubated for 30mins at 37°C. Reaction was deactivated by 10% FBS. The solution was then passed through a 40 μm cell strainer. After centrifugation at 400 g for 5 mins, cell pellet was incubated with 1ml of RBC lysis buffer on ice for 3 mins. Cell number and viability were analyzed using Countess AutoCounter (Invitrogen, C10227). This method generated single cell suspension with greater than 80% viability.

Single-cell RNA Sequencing

Single cell RNA sequencing was performed as described in our previous study (Park et al., 2018). Briefly, the single cell suspension was loaded onto a well of a 10x Chromium Single Cell instrument (10x Genomics). Barcoding and cDNA synthesis were performed according to the manufacturer's instructions. Qualitative analysis was performed using the Agilent Bioanalyzer High Sensitivity assay. The cDNA libraries were constructed using the 10x Chromium™ Single cell 3' Library Kit according to the manufacturer's original protocol. Libraries were sequenced on an Illumina HiSeq or NextSeq 2x150 paired-end kits using the following read length: 26bp Read1 for cell barcode and UMI, 8bp I7 index for sample index and 98bp Read2 for transcript.

Alignment and Generation of Data Matrix

Cell Ranger 2.0 (http://10xgenomics.com) was used to process Chromium single cell 3' RNA-seq output. First, ''cellranger count'' aligned the Read2 to the mouse reference genome (mm10) and exons of protein coding genes (Ensembl GTFs GRCm38.p4). Sequencing reads that were marked by multiple mapping were removed by adjusting the cellranger to unique mapping (marked MM:i:1 in the bam files). Third, the fastq files extracted from bam files of the first run were used again for ''cellranger count'' to generate data matrix. Finally, the output files for 6 normal and 2 FAN samples were aggregated into one gene-cell matrix using ''cellranger aggr'' with read depth normalization by total number of mapped reads.

Data Quality Control, Preprocessing and Dimension Reduction

Seurat R package (version 2.3.4) was used for data QC, preprocessing and dimension reduction analysis. Once the gene-cell data matrix was generated, poor quality cells were excluded, such as cells with < 200 or > 3,000 expressed genes. Genes that were expressed in less than 10 cells, mitochondrial genes, ribosomal protein genes and HLA genes, that were reported to induce unwanted batch effects, were removed for further analysis (Smillie et al., 2019). Cells were also discarded if their mitochondrial gene percentages were over 50%. The data were natural log transformed and normalized for scaling the sequencing depth to a total of 10,000 molecules per cell, followed by regressing-out the number of UMI and genes. Batch effect was corrected by using removeBatchEffect function of edgeR. The expression values after batch correction were only used for PCA, t-Distributed Stochastic Neighbor Embedding (tSNE) visualization and clustering, and the original expression values before batch correction were used for all downstream analyses such as identification of marker genes and differentially expressed genes. For the dimension reduction, highly variable genes across the single cells were identified using 0.0125 low cutoff and 0.3 high cutoff. PCA was performed using the variable genes as input and top 20 PCs were used for initial tSNE projection.

Removal of Doublet-like Cells

Doublet-like cells were identified using DoubletFinder which is a computational doublet detection tool with following parameters: proportion.artificial = 0.25 and proportion.NN = 0.01(McGinnis et al., 2019). Then, the number of expected doublets were calculated for each sample based on expected rates of doublets, which are provided by 10x Genomics. After removing the doublet-like cells, all steps including normalization, regressing out variables, batch effect removal, and dimension reduction were performed again.

Cell Clustering Analysis

Density-based spatial clustering algorithm, DBSCAN, was used to identify cell clusters on the tSNE plot with the eps value 0.4. Clusters were removed if their number of cells was less than 20. Proximal tubule clusters expressing a proximal tubule marker, *Slc27a2*, were separated from the rest of cell clusters in order to identify subgroups. PCA and UMAP (Uniform Manifold Approximation and Projection) were performed only for the remaining cells. DBSCAN was used to identify cell clusters on the UMAP plot with initial setting for the eps value 0.5. Each of the resulting clusters was subjected to sub-clustering by a shared nearest neighbor (SNN) modularity optimization-based clustering algorithm, which is implemented in Seurat package. Resolution 0.5 was used for sub-clustering of the clusters except T lymphocytes which required higher resolution (0.7) to identify T lymphocyte subgroups. Post-hoc differential expression analysis was performed for every pair of sub-clusters. Sub-clusters were merged when they had 15 or less than 15 (10 differential genes for T lymphocytes) differentially expressed genes (average expression difference > 1 natural log with an FDR corrected $p<0.01$). This clustering analysis resulted in 30 cell clusters. PT cell clusters were also subjected to sub-clustering. With same procedure used for other clusters, PT cells from control and FAN samples were subclustered into 5 and 9 sub-cell types, respectively.

Mouse Bulk RNA-sequencing Analysis

Total RNAs were isolated using the RNeasy mini kit (Qiagen). Sequencing libraries were constructed using the Illumina TruSeq RNA Preparation Kit. High-throughput sequencing was performed using Illumina HiSeq4000 with 100bp single-end according to the manufacturer's instruction. Adaptor and lower-quality bases were trimmed with Trim-galore. Reads were aligned to the Gencode mouse genome (GRCm38) using STAR-2.4.1d. The aligned reads were mapped to the genes (GRCm38, version 7 Ensembl 82) using HTSeq-0.6.1. Differentially expressed genes between control and disease groups were identified using DESeq2 version 1.10.1. To examine the enrichment of the differentially expressed genes in single cell clusters, a z-score of normalized expression value was first obtained for every single cell. Then, we calculated the mean z-scores for individual cells in the same cluster, resulting in 30 values for each gene. The z-scores were visualized by heatmap showing the enrichment patterns of the genes across the cell types.

Estimation of Cell Proportions

From single cell datasets, the numbers of cells in each cluster were enumerated and normalized by total number of cells for each condition (6 control and 2 diseased samples). Since a number of PT cells in FAN samples showed higher expression of apoptosis markers, we removed the cells that express *Bax, Bad* or *Dap* from all samples only for the cell proportion test. Deconvolution of bulk RNA sequencing data was performed to validate the cell proportion changes that were detected in single cell data. CellCODE package was used for deconvolution using 30 cell type-specific marker genes (Chikina et al., 2015).

Identification of Marker Genes and Differentially Expressed Genes

Conserved marker genes between control and UUO samples were identified using FindConservedMakers function of Seurat with default options. Average expression difference > 0.5 natural log and FDR corrected p value < 0.01 were applied. Cell type-specific differentially expressed genes were identified using MAST, which is implemented in Seurat package with log fold change threshold = 0.2, minimum percent of cells expressing the genes=0.05 and adjusted p value < 0.05.

Cell Trajectory Analysis

RNA Velocity

To calculate RNA velocity, Velocyto.R package was used as instructed (La Manno et al., 2018). We used Velocyto to impute the single-cell trajectory/directionality using the spliced and the unspliced reads. Resulting loom files were merged and loaded into R following the instructions. Furthermore, RNA velocity was estimated using gene-relative model with k-nearest neighbor cell pooling (k = 25). To visualize RNA velocity, we performed Principle Component Analysis and used the top 20 principle components to calculate UMAP embedding. The parameter n was set at 200, when visualizing RNA velocity on the UMAP embedding.

Monocle2

To construct single cell pseudotime trajectory and to identify genes that change as the cells undergo transition, Monocle2 (version 2.4.0) algorithm was applied to the cells from proximal tubules and proliferating proximal tubules (Trapnell et al., 2014). To show the cell trajectory from the small cell population (proliferating proximal tubules) to predominant cell type (proximal tubules), 6,000 randomly selected PT cells and proliferating proximal tubules were used for Monocle analysis. Genes for cell ordering were selected if they were expressed in $\geq$ 10 cells, their mean expression value was $\geq$ 0.05 and dispersion empirical value was $\geq$ 2. Highly variable genes along the pseudotime were identified using differential GeneTest function of Monocle2 with q-value < 0.01. The trajectory analysis was also performed for precursors and PST cells from the control and FAN samples separately. DAVID GO term analysis was performed for the highly variable genes along the control and FAN trajectory, and then genes in the lipid metabolism GO term were visualized by heatmap.

Single Cell ATAC Sequencing Analysis

Data matrix for PCT and PST cells-specific open chromatin regions was downloaded (Cao et al., 2018). HOMER package was used to identify known transcription factor binding motifs that are highly enriched in the PCT and PST-specific open chromatin regions. GSEA package was used to determine the enrichment patterns of ESRRA binding genes in differentiated PT cells and to identify core enrichment genes.

Human Bulk Gene Profiling Data Analysis

Kidney samples were collected from nephrectomies. Samples were permanently deidentified and clinical information was collected by an honest broker, therefore the study was deemed exempt by the institutional review board (IRB) of the University of Pennsylvania. Two datasets were used, one dataset included 91 human kidney samples and gene expression analysis was performed using Affymetrix U133A arrays (E-MTAB-2502) (Table S7) Raw expression levels of microarray data sets were normalized using the RMA algorithm and log transformed. The identified marker genes were used as an input for CellCODE deconvolution analysis to estimate the cell proportion changes in human patient kidney samples. To assess the effect of cell proportions changes on the correlation between gene expression and fibrosis score, we implemented linear regression models using age, gender, race and diabetes and hypertension status as covariates with and without cell proportions of PCT, PST, myeloid and lymphoid cells. The second dataset included 431 samples and gene expression was analyzed using RNAseq (Table S7).

Single Cell Suspension from Kidney organoid

Day 20 mature kidney organoids were washed twice with PBS and incubated first with AccumaxTM for 10 min at 37°C, followed by Trypsin-EDTA 0.25% incubation in order to dissociate into single cells. Cells were spun down at 400 g for 5 min resuspended in ADV RPMI and checked for viability using Countess Automated Cell Counter.

Mitotracker Green FM Flow Cytometric Analysis

Developing kidney organoids on day 14 of differentiation were cultured in EGM or REGM media for 4 additional days. In order to assess mitochondrial mass, organoids were stained with MitoTracker Green FM (100 nM), a mitochondrial specific fluorescent dye at 37°C for 30 min. After incubation, kidney organoids were washed twice with PBS and disaggregated into single cell suspension using AccumaxTM for 10 minutes followed by Trypsin-EDTA 0.25% (ThermoFisher) incubation for at least 10 minutes at 37°C. Once cells dissociated, FACS buffer (PBS supplemented with 5% of FBS) was added to cease the trypsin activity and samples were centrifuged for 5 minutes at 1800 rpm. After removing the supernatant, the pellet was resuspended in 300 μl of FACS buffer and the suspension was filtered into FACS tubes. Nuclei were stained with DAPI (ThermoFisher). Cells were counted using FACS Aria Fusion Instrument (BD Biosciences). FlowJo software version 10 was used for data analysis.

Protein Extraction and Western Blot Analysis in Kidney Organoids

Protein was extracted from kidney organoids cultured in EGM or REGM media for 4 days using RIPA buffer (Thermofisher) supplemented with complete protease inhibitor cocktail (Thermofisher), and centrifuged at 13,000 g for 15 mins at 4°C. The supernatant was collected, and protein concentration was measured using a bicinchoninic acid (BCA) protein quantification kit (Thermo Scientific). For western blot analyses, 25 ug of protein were separated in 10% sodium dodecyl sulphate-polyacrylamide gel (SDS-PAGE) and blotted onto nitrocellulose membranes. Membranes were blocked at room temperature for 1 hour with TBS 1X- 5% BSA. Membranes were then incubated in primary antibody (dilution 1:1000) Total OXPHOS cocktail (Abcam) overnight at 4°C. The membranes were then washed with PBST (PBS1X + 0.05% Tween20; Merck) for 5 minutes three times and incubated with anti-mouse secondary antibody (dilution 1:10,000) (IRDye®680RD Goat anti-Mouse; LI-COR). After washing with PBST for 5 minutes twice and with PBS for 5 minutes once, membrane-bound antibodies were detected by fluorescence with the Odyssey ® Fc Imaging System. Alpha-tubulin (1:5000; Sigma) was used as a loading control for normalization and quantification. Images were analyzed with Image Studio Lite Version 5.2 software.

Immunofluorescence

Kidney organoids were cultured in EGM or REGM media were transferred to 96 well plates. Fixation was performed with paraformaldehide 4% (Thermo Fisher) for 20 minutes followed by 10 minutes washing in three changes PBS. Kidney organoids were incubated in Streptavidin/Biotin Blocking Kit (Vector Laboratories) and TBS – 1% triton + 6% donkey serum for 2 h at room temperature. Podocalyxin (PODXL, Dilution 1:250) and LTL (Dilution 1:200) antibodies were diluted in TBS-0.5% Triton + 1% BSA. Kidney organoids were then treated overnight at 4°C with primary antibodies. The next day, organoids were washed with TBS-0.5% triton + 1% BSA for 5 minutes three times and incubated with secondary antibody (Dilution 1:500) in TBS-0.5% Triton + 1% BSA at room temperature for 2 hours. Subsequently, organoids were washed with TBS twice for 5 minutes and nuclei were stained with DAPI (Dilution 1:5000) for 10 minutes. Organoids were collected with special wide-end tips, and placed on slides and mounted with Fluoromount-G (Southern Biotech). Confocal images were acquired using Leica SP5 microscope and LTL positive cells were analyzed using ImageJ.

Mitochondrial DNA Analysis

MtDNA copy number is represented by the ratio of mitochondrial DNA to nuclear DNA (mtDNA/nDNA). Total DNA was isolated from LTL^+ PT cells 48 hours after transfection using DNeasy Blood & Tissue Kit. The mtDNA/nDNA ratio was determined by quantifying two

mitochondrial genes (16S rRNA and ND1) and two nuclear genes (HK2 or 18S rRNA) using qPCR (Quiros et al., 2017). The primer sequences are listed in Table S6.

PT Cell Transfection

PT cells were transfected with Non-targeted (NT) siRNA or si*Esrra* (purchased from Dharmacon) and pcDNA3.0 (vector) or pAd-Track-Esrra/pcDNA3.1-Ppara/pcDNA3.1-HNF1A/pAd-track-HNF4A (overexpression constructs) (kind gift from Dr. Liming Pei, University of Pennsylvania). siRNA and plasmid transfections were performed using Lipofectamine 3000. For transfection, cells were seeded in 6-well plates, grown for overnight until 60–70% confluent, and then transfected with 100nM (final concentration) *siRNA/siEsrra* and 5μg of vector/ESRRA/PPARA/HNF1B/HNF4A overexpression plasmids. Transfection efficiency was determined under fluorescence microscope by the presence of Cy3 transfection control (data not shown). Cells were harvested and scraped off 48 h post transfection under different condition.

Oxygen Consumption Rate (OCR)

The measurement of OCR in PT cells transfected with si*Esrra* or ESRRA plasmid were performed using XFe96 extracellular flux analyzer (Seahorse Bioscience) as previously described (Kang et al., 2015). Briefly, PT cells were plated at density of 10,000 cells/well in a Sea-horse cell culture microplate and transfected with si*Esrra*/ESRRA OE. Cellular OCR was measured 48 h post-transfection and normalized to protein quantity in each well. The final concentration for oligomycin, FCCP, rotenone and antimycin used was 2 μM, 1 μM, 1 μM and 1 μM, respectively.

Chromatin Immunoprecipitation qPCR

ChIP was performed to evaluate enrichment of ESRRA binding regions in targets SLCs genes in PT cells following the manufacturer's instructions (492024, Invitrogen). Briefly, 10^7 PT cells were cross-linked with 1% formaldehyde for 10 min at room temperature. Then the reaction was stopped by adding glycine (final concentration, 0.125M). The cells were sonicated in lysis buffer to achieve a chromatin size of 100–500 bp. The sonicated chromatin was diluted by using dilution buffer. 5 μg ESRRA/IgG antibody was coupled with Dynabead protein A and G (1:1 mixed), the mixture was incubated with chromatin lysates overnight at 4 °C with rotation. Immune complexes were washed with IP buffers. Antibody-bound chromatin was reverse-cross-linked, and the ChIP DNA samples were purified for PCR reaction. Primers used for ChIP-qPCR are shown in Table S6.

Fenofibrate Treatment

LTL^+ PT cells isolated from mouse kidneys were cultured in either presence of 1μM fenofibrate (PPARA agonist) to activate PPARA or DMSO in primary culture media from Day 0. Cells were harvested for RNA and protein isolation for Western Blot on Day 7.

XCT790 Treatment

Kidney organoids cultured in REGM media for 7 days were treated with 10μM of XCT790 for 48 hours followed by immunostaining or RNA isolation. Human proximal tubule cells (HPTC) and LTL^+ mouse PT cells were cultured in REGM media and treated with 10 μM of XCT790 or DMSO for 48 hours and 24 hours respectively.

qRT-PCR

RNA was isolated from cells, kidney organoids and kidneys tissue using Trizol (Invitrogen). 2 μg RNA was reverse transcribed using the cDNA archival kit (Life Technologies), and qRT-PCR was run in the ViiA 7 System (Life Technologies) machine using SYBRGreen Master Mix (Applied Biosystem) and gene-specific primers. The data were normalized and analyzed using the ΔΔCt method. The primers sequences used are shown in Table S6.

Western Blot

Cells were lysed in radioimmunoprecipitation assay buffer (RIPA; Cell Signaling Technology) and protein was quantified by BCA method (Thermo Fisher Scientific). Protein samples (10 to 30 μg) were separated by SDS-PAGE and then transferred to PVDF membranes. After blocking, for 30 min with 5% milk in TBST and three times washing, membranes were incubated overnight with primary antibody (COX IV 1:1000, OXPHOS 1:250, GAPDH 1:2000, PGC1a 1:500, SLC6A13 1:1000, SMA 1:1000, FN 1:1000, ESRRA 1:2000, β-actin 1:20,000) in TBST (see KRT). After three washes for 5 min, membranes were incubated for 45 min at RT to 1 hour with secondary HRP-conjugated antibody (1:20,000) in TBST. The signal was developed with Immobilon forte western HRP substrate (Milipore) and measured using Odyssey®Fc Imaging System (*LICOR*) equipment and software. The following antibodies were used in this study are listed in Key Resources Table.

Histological Analysis

Kidneys samples were fixed in 10% neutral formalin and paraffin-embedded sections were stained Periodic acid–Schiff (PAS) and hematoxylin and eosin (H&E) to analyze the histology of samples. Sirius-red staining (Boekel Scientific, #147122) was performed to determine the degree of fibrosis. We performed immunocyto- and -histochemistry on paraformaldehyde fixed cells and formalin-fixed, paraffin-embedded kidney sections. We used the following primary antibodies: ESRRA (1:200), SLC6A13 (1:100), SLC34A1 (1:100), and SLC7A13 (1:100). Staining was visualized using peroxidase-conjugated antibodies to mouse immunoglobulin using

the Vectastain Elite kit and 3,3-diaminobenzidine (DAB) (Vector Labs). For cell proliferation, we used Ki67 (1:150) primary antibody and Alexa Fluor 555 as secondary antibody, and nuclei was stained by Hoechst dye.

QUANTIFICATION AND STATISTICAL ANALYSIS

Data Representation and Statistical Analysis

Student's t-test was used to analyze differences between two groups, and One-way or Two-way ANOVA was used to analyze inter-group differences (tukey's multiple comparisons test). *P*-values less than 0.05 were considered statistically significant. The analysis was performed using GraphPad Prism 5 (GraphPad software). Densitometry results of Western Blots were quantified using ImageJ software. All data are presented as mean ± SEM and other details such as the number of replicates and the level of significance is mentioned in figure legends and supplementary tables. For mice experiments, animals were randomly allocated to different groups prior the experiments. No samples or animals were excluded from analysis. Sample size estimation was not performed, and sample size was determined based on the number of available age and gender matched animals in the colony. For single-cell data analysis, statistical details are provided in designated method section. All samples were processed in blinded fashion.